# Reaction Heterogeneity in LiFePO<sub>4</sub> Agglomerates and the Role of Intercalation-Induced Stress

Fan Wang<sup>1†</sup>, Kaiqi Yang<sup>1†</sup>, Mingyuan Ge<sup>2</sup>, Jiajun Wang<sup>2,3</sup>, Jun Wang<sup>2</sup>, Xianghui Xiao<sup>2</sup>, Wah-Keat Lee<sup>2</sup>, Linsen Li<sup>4</sup>, Ming Tang<sup>1\*</sup>

- Department of Materials Science & NanoEngineering, Rice University, Houston, TX 77005, USA
- National Synchrotron Light Source II, Brookhaven National Laboratory, Upton, NY 11973, USA
- School of Chemistry and Chemical Engineering, Harbin Institute of Technology, 150001, Harbin, China
- 4. Department of Chemical Engineering, Shanghai Electrochemical Energy Device Research Center (SEED), Shanghai Jiao Tong University, Shanghai, 200240, China

<sup>†</sup> These authors contribute equally.

<sup>\*</sup>Corresponding author email: mingtang@rice.edu

### **Abstract**

As an important battery cathode material, reaction distribution in lithium iron phosphate (LiFePO<sub>4</sub>) has been extensively studied in dispersed particle systems, but remains poorly understood for mesoscopic agglomerates (or secondary particles) that are used in most commercial batteries. Herein, we apply three-dimensional X-ray spectroscopic imaging to characterize the two-phase structure in LiFePO<sub>4</sub> secondary particles during electrochemical cycling. (De)lithiated domains are found to not form the commonly assumed core-shell structure but develop highly anisotropic filamentary morphology that is rate independent and symmetric between charging and discharging. Phase-field simulations elucidate that the observed 1D phase growth behavior is not caused by the 1D lithium diffusivity of LiFePO<sub>4</sub> but the elastic interaction between primary particles, which gives rise to stronger reaction heterogeneity than dispersed nanoparticles. As a result, uniform lithium (de)intercalation does not occur on the secondary particle surface even at high cycling rates.

During battery operation, the state of charge (SOC) of the active material usually have heterogeneous spatial distributions within the electrodes at multiple length scales from the particle to cell level<sup>1</sup>. The development of such non-uniform reaction distributions is undesirable because it increases cell polarization, reduces capacity utilization, induces local over-(dis)charge and generates stress concentration that promotes electrode fracture. Advances in characterization techniques in recent years have allowed researchers to probe this phenomenon and its origins in great details. A comprehensive review on this topic can be found in ref. <sup>1</sup>. Improving the reaction uniformity within battery electrodes is an effective way to enhance battery performance, safety and cycle life <sup>2-5</sup> without relying on new materials and electrode chemistry.

Existing studies reveal that many factors contribute to the SOC heterogeneity in battery electrodes. These include but are not limited to sluggish electronic and ionic transport <sup>6-8</sup>, slow Li diffusion in the active materials <sup>9-12</sup>, polycrystalline structure of the active materials <sup>4,13,14</sup>, the SOC dependence of the equilibrium electrode potential <sup>2,3,5,15</sup>, non-uniform electrical contact <sup>16,17</sup>, orientation-dependent surface reaction kinetics <sup>18,19</sup>, instability of intercalation fronts <sup>20,21</sup>, and electro-autocatalysis <sup>22,23</sup> etc.

For phase separating electrode materials like LiFePO<sub>4</sub>, the SOC distribution is closely related to the phase transformation process during (dis)charging and exhibits distinct characteristics at different particle sizes. (De)intercalation in dispersed LiFePO<sub>4</sub> nanoparticles at low to intermediate rates is nucleation-limited<sup>24,25</sup>: the new phase exhibits facile growth within the particle once it overcomes the nucleation energy barrier, and the majority of the particles are in either the LiFePO<sub>4</sub> (LFP) or FePO<sub>4</sub> (FP) single phase, exhibiting the "particle-by-particle" intercalation behavior<sup>25</sup>. On the other hand, reaction distribution in microsized LFP single crystals is controlled by bulk lithium diffusion, with the FP (or LFP) phase preferentially expanding along the particle surface but growing slowly into the particles due to the diffusion limitation<sup>11,12</sup>. A FP/LFP core-shell structure has been observed at intermediate SOCs<sup>11</sup>.

Because of their structure simplicity, well-separated or loosely connected LFP nano- and microcrystallites have been extensively employed in the study of the reaction and phase transition behavior of this important cathode material. Electrodes used in commercial Li-ion batteries, however, are usually made of microsized agglomerates or secondary particles consisting of many nanoscale primary particles in order to achieve high packing density and volumetric energy density. Unlike dispersed nanoparticles of similar size, primary crystallites in a secondary particle interact with each other through direct lithium exchange and elastic stress caused by Li-insertion-induced volume changes. Compared to microsized single crystals, the polycrystalline nature of the secondary particles will significantly influence the Li transport pathways and the internal stress state. These dissimilarities are likely to result in unique reaction behavior in LFP agglomerates that differ from dispersed particles, which nonetheless has received little attention<sup>26</sup> despite its practical importance.

In this work, we apply full-field transmission X-ray microscopy (FF-TXM) in combination with X-ray absorption near-edge structure (XANES) spectroscopy and tomographic reconstruction to directly visualize the phase and SOC distributions of partially (de)lithiated LFP secondary particles in 3D with nanoscale resolution. FF-TXM with XANES / nanotomography has seen successful applications to various battery electrode systems in recent years, which provide valuable insights on the reaction heterogeneity and degradation mechanisms<sup>4,11-14,19,27-31</sup>. 3D phase mapping from our experiments reveals the formation of filament-shaped FP / LFP domains in secondary particles upon (de)lithiation, which to our knowledge has not been reported before and represents a significant departure from the commonly assumed core-shell reaction geometry. These domains have large aspect ratios and diameters smaller than the primary particle size. They persist over a wide range of SOCs and are independent of the charging rate. The observed filamentary phase morphology is well reproduced by phase-field simulations, which confirm the important role of the LFP/FP misfit stress and the misorientation between primary particles in controlling the nucleation and growth process in secondary particles. The combined experimental and modeling study reveals that the elastic interaction between primary particles could result in strong reaction heterogeneity at the agglomerate-level, which may also apply to other electrode systems.

The LFP used in this study was a commercial product from a cathode producer (BTR). Its charge/discharge curves are shown in Supplementary Figure S1. The LFP primary particles in the sample

are ~240 nm in diameter as measured from SEM, and the secondary particle size is in the range of 2-10 µm (Figure 1a). SEM and tomography show that large secondary particles have a significant volume fraction of pore space. Here we focus on smaller secondary particles (2-5 µm) with a much lower internal porosity (Figure 1b). A criterion of internal porosity less than 5% is used in choosing the particles for detailed analysis in this work. To obtain 3D mappings of LFP vs FP phases in secondary particles, a series of nano-tomography datasets were collected from the same region of LFP electrodes at different incident X-ray energies across the Fe K-edge (7112 keV). One absorption-contrast 3D tomographic image was reconstructed from each energy level. They were carefully aligned to yield a XANES spectrum for each voxel ( $40 \times 40 \times 40 \text{ nm}^3$ ) occupied by the active material in the imaged region. The large field of view ( $50 \times 50 \times 40 \text{ µm}^3$ ) of FF-TXM allows multiple particles to be imaged in one scan. The local fractions of the LFP and FP phases in a voxel are quantified by fitting the spectrum with a linear combination of the LiFe<sup>2+</sup>PO<sub>4</sub> and Fe<sup>3+</sup>PO<sub>4</sub> reference spectra as shown in Figure 1c, which generates a mapping of phase fraction within the particles like the one shown in Figure 1d.

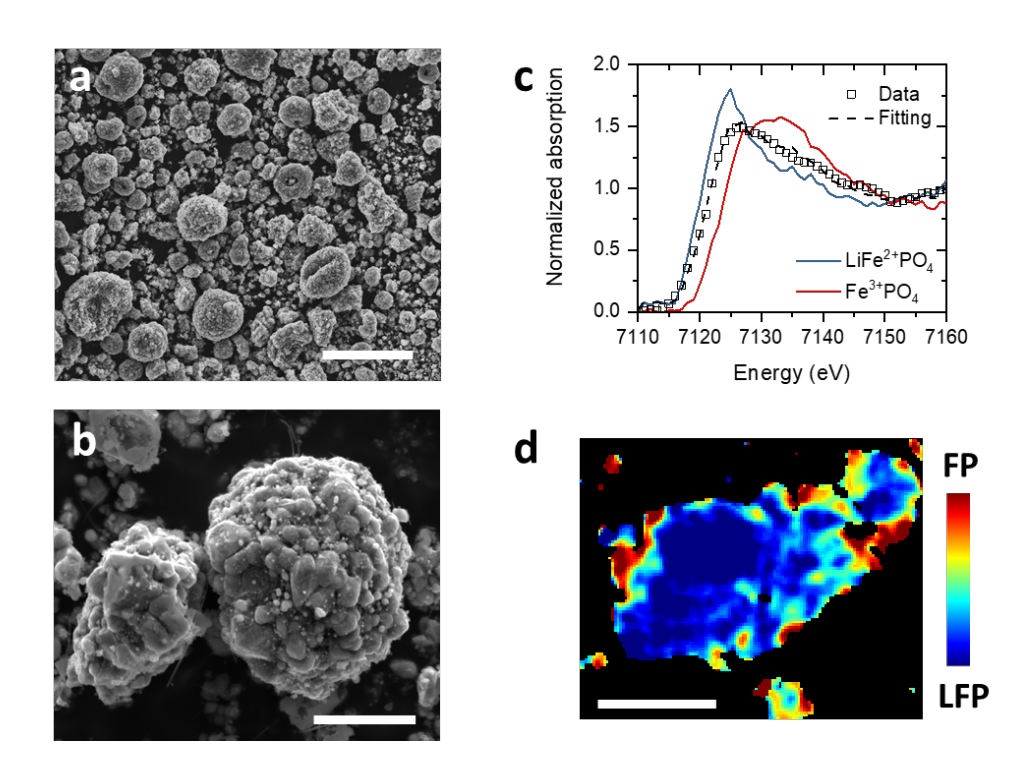


**Figure 1. SEM and XANES imaging of LFP secondary particles. a, b)** SEM photos of the commercial LFP secondary particles used in this study. **c)** XANES spectra of LiFe<sup>2+</sup>PO<sub>4</sub> (blue line), Fe<sup>3+</sup>PO<sub>4</sub> (red line) and a mixed LFP/FP region (squares) as well as its fitting (dashed line) by the reference spectra. **d)** A cross-section of the 3D chemical mapping of a partially charged LFP secondary particle that visualizes the local FP/LFP phase fraction. Scale bar: a. 20 μm; b and d. 2 μm.

We investigated the LFP/FP phase distribution in secondary particles from partially (dis)charged samples. Several secondary particles from electrodes charged to a global SOC of 25% at a rate of 0.1C or 2C (nC = full charge in 1/n hours) are shown in Figure 2a and b, respectively, in which a particle voxel is labeled as LFP (or FP) if its LFP phase fraction is larger (or smaller) than 50%. Supplementary Figure S2 shows the distribution of the internal pore phase within these particles, the porosity of which is 3.4% (Figure 2a) and 4.2% (Figure 2b), respectively. The particles from the 0.1C sample have an average SOC of 31.4%, and those from the 2C sample have an average SOC of 30.5%. Strong SOC heterogeneity is clearly present on the particle surface in both samples. The FP phase does not uniformly cover the particle surface as commonly assumed but forms separate domains. Such behavior differs from single crystalline LFP particles of comparable size 11, in which the development of the core-shell phase morphology was observed. There is no significant correlation between the FP domains and the local particle surface curvature (see Supplementary Figure S3), which suggests that particle geometry does not play a major role in the nucleation of the new phase. A close examination of individual FP domains in many particles from the samples reveals that they display filament-like features with large aspect ratios, which indicates highly anisotropic growth of the FP phase in secondary particles. We emphasize that the filamentary structure is not an artifact of voxel binarization as similar domain morphology can be readily observed from the unbinarized version of the 3D phase fraction mapping as shown in Supplementary Figure S4.

We further applied filament tracing analysis to quantify the morphology of the FP domains, which was performed with the XFiber Module in the visualization software Avizo 9.0 <sup>32</sup>. The analysis utilizes a tracing algorithm to compute the cross correlation between the tomograph and cylindrical templates <sup>33</sup>, from which the centerline of the FP domains is extracted. Each FP segment between the triple joints on the centerline is approximated as a tortuous tube with the same volume, and its geometrical features such as tube lengths

and diameters are calculated. As illustrated in Figure 2c and d, FP domains in the secondary particles shown in Figure 2a and b are well represented by separated or interconnected tubes generated by the analysis. A total of 297 individual FP tubes are identified by the analysis for the secondary particles from the 0.1C-charging sample (Figure 2a). Figure 2e shows that the length-to-diameter ratio of these tubes spans from 1 to 23 with an average value of 6.1, which confirms the large anisotropy of the FP filaments. On the other hand, the average tube diameter (136 nm) is only 0.57 times of the average primary particle size (240 nm measured from SEM images) in the secondary particles (Figure 2f). This result implies a 1D growth process of the FP phase during delithiation, in which the FP filaments could expand over multiple primary particles along the axial direction but are largely confined within a single primary particle in their radial directions. The filament geometry suggests that intra- and inter-primary-particle heterogeneities must co-exist in secondary particles, with some primary particles containing both LFP and FP phases. The FP domains in the secondary particles from the 2C-charged sample (Figure 2b) exhibit similar length-to-diameter ratio and diameter distributions (Figure 2g and h), with their respective means being 6.9 and 0.56. The morphology of the FP phase that develops in LFP secondary particles appears to be insensitive to the charging rate.

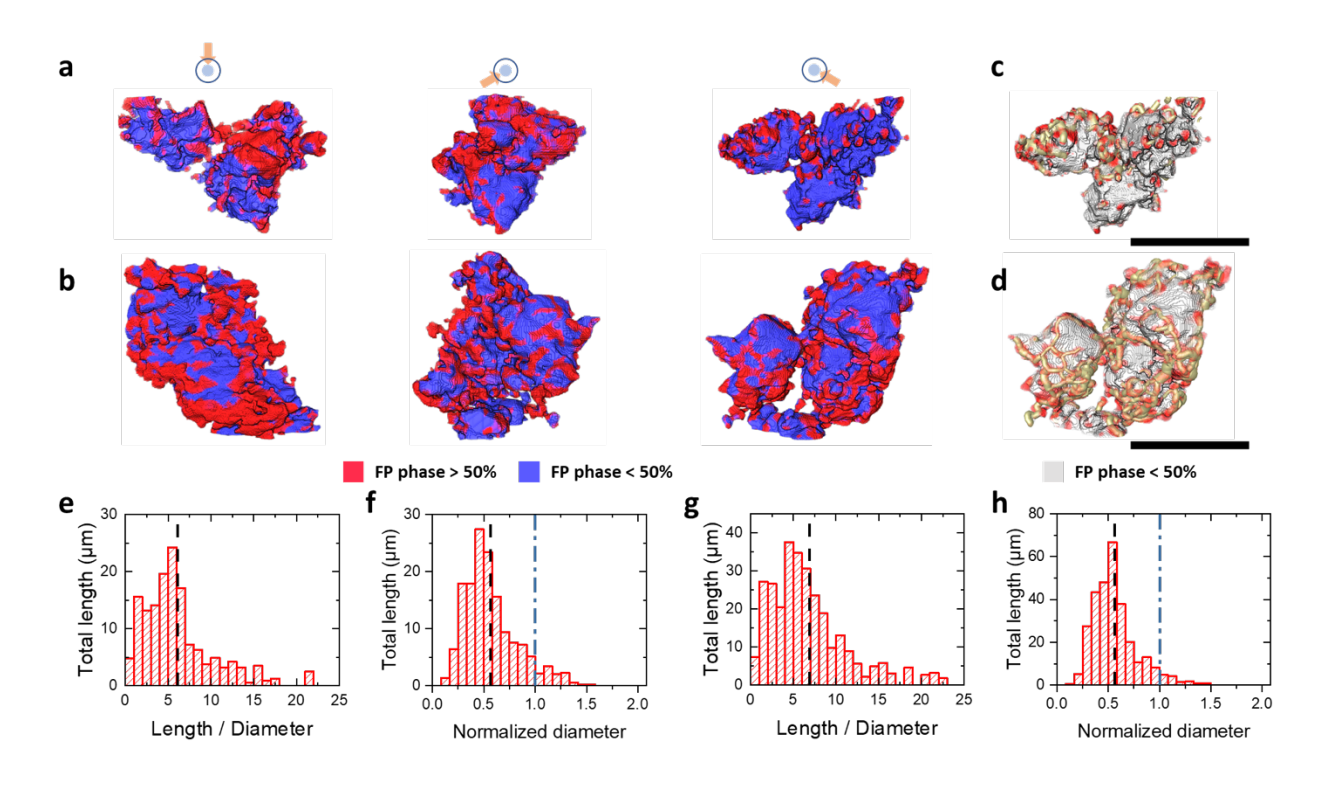


Figure 2. Filamentary FP domains in partially delithiated LFP secondary particles. a, b) Binarized phase mapping (red – FP voxels, blue – LFP voxels) of secondary particles from LFP cathodes charged to a global SOC of 25% at 0.1C and 2C, respectively. The same particles are viewed from different directions as indicated by the arrows. c, d) Tubular representation of the FP domains in the particles shown in a and b, respectively. Yellowish tubes generated by the filament tracing analysis are superimposed on FP domains in semi-transparent red. e, g) Histograms of the FP tube length/diameter ratio in the particles shown in c and d, respectively, with the black dashed line representing the average ratio. f, h) Histograms of the FP tube diameters normalized by the average primary particle size in the particles shown in c and d, respectively. The black dashed line indicates the average tube diameter. Scale bars in a and b are 5 μm.

To obtain more insights on the nucleation and growth process, we examined the phase distribution in secondary particles with varied SOCs. Figure 3a and b shows a total of 18 particles whose particle-level SOC ranges between 6% and 94% from samples charged at a rate of 0.1C and 2C, respectively. Three additional particles with local SOC = 6%, 30% and 63% are visualized in Supplementary Figure S5-S7. In particles with local SOC < 10%, FP domains only exist on particle surface (also see Supplementary Figure S5), suggesting that the FP phase is surface-nucleated. Upon increasing SOC, FP nuclei extend into filaments and maintain the tubular morphology over a wide range of SOCs. A close look at the spatial distribution of FP domains in particles with SOCs between 20% and 50% show that the majority of them are confined near the particle surface, which implies that they preferentially grew along the surface, although some filaments do extend into the particle interior (Supplementary Figure S6b). When the particlelevel SOC rises beyond 60%, individual FP domains start to coalesce with each other and form continuous surface coverage, which resembles the core-shell two-phase structure, see Supplementary Figure S7. We also found that the phase evolution exhibits symmetry between charging and discharging. LFP domains formed upon particle lithiation develop similar filamentary morphology. This can be seen in Figure 3c, which shows several particles from a sample discharged to a global SOC of 50% at 0.1C. Filament tracing analysis confirms that the LFP filaments also have an average diameter below the primary particle size.

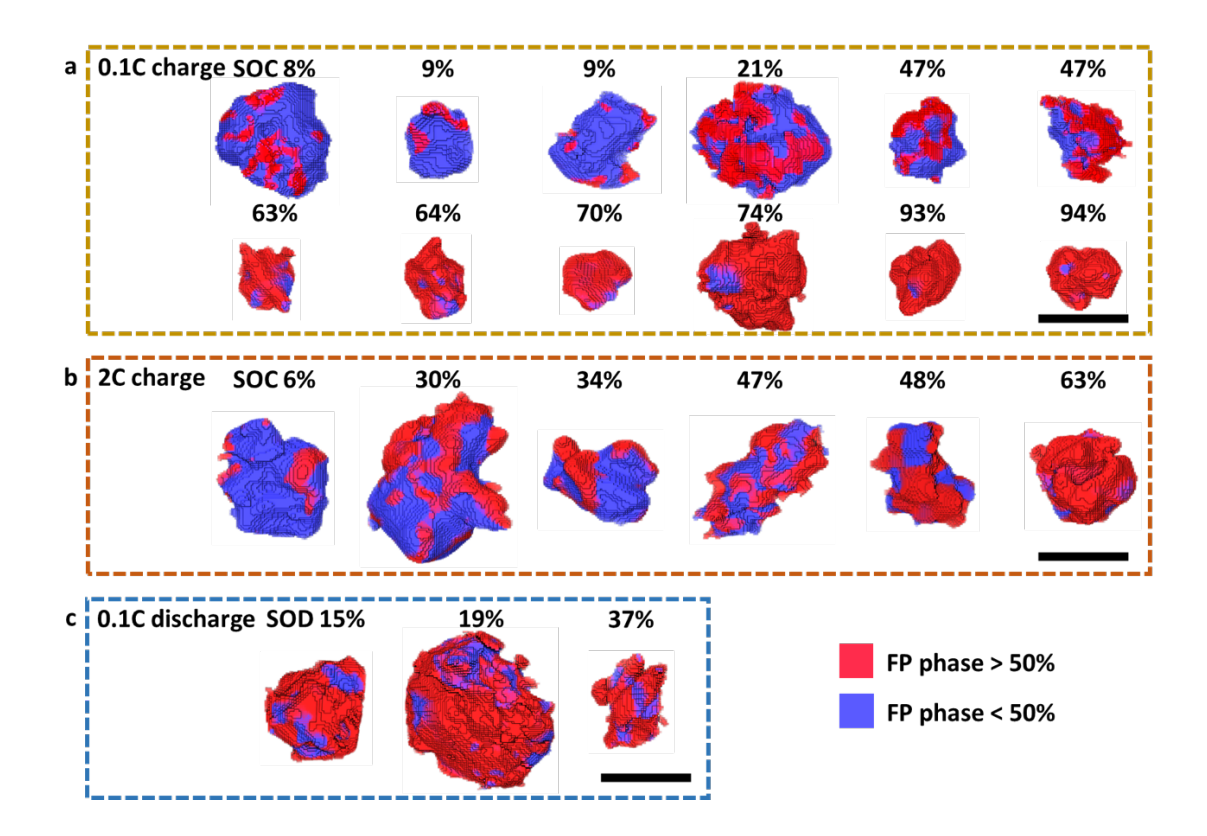


Figure 3. 3D phase mappings of partially (de)lithiated LFP secondary particles with different particle-level SOCs or states of discharge (SOD). a, b) Particles from partially delithiated electrodes charged at 0.1C and 2C, respectively. c) Particles from a partially lithiated electrode discharged at 0.1C. Scale bars are  $2 \mu m$ .

As the 3D XANES measurements were conducted ex-situ, it is reasonable to question whether the observed phase distribution could have developed during rest after (dis)charging was terminated. Since the electrodes examined in this study were quickly removed from battery cells and dried after (dis)charging, lithium redistribution between secondary particles in the electrodes is expected to be negligible. Nevertheless, Li exchange between primary particles within the same agglomerate could still occur through bulk or surface<sup>34</sup> diffusion, which may result in further phase evolution during rest. To rule out this possibility, we performed operando 2D XANES imaging of an LFP cathode in an in-situ coin cell, which was potentiostatically charged at 3.46V. The electrode was fully delithiated in about 12 hours, which is comparable to a charging rate at 0.1C. Figure 4 shows the 2D phase mapping of a secondary particle at different times during charging, in which the local phase fraction is depth-averaged along the beam direction. Discrete reaction "hotspots" can be seen inside the particle at the early charging stage (1.8h, 3h).

The FP phase nucleated at these locations subsequently grew and formed elongated morphology, which resembles the 1D domain structure observed in the 3D XANES measurement. Supplementary Figure S8 shows another particle from a different region with similar non-uniform reaction behavior. The operando measurement supports that 1D phase growth occurs in LFP secondary particles during the (dis)charging process.

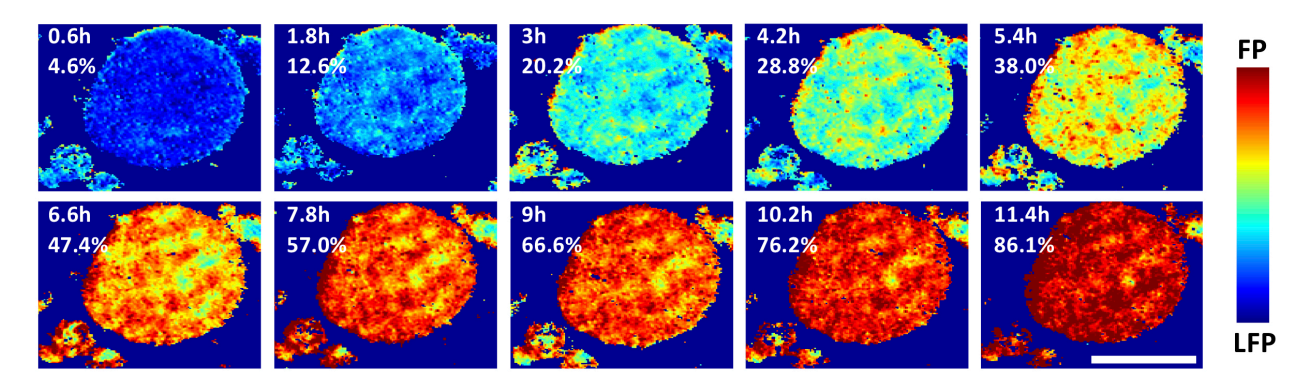


Figure 4. Operando 2D phase mappings of a secondary particle in an LFP electrode at different times during potentiostatic charging at 3.46 V. Time and the corresponding SOC of the secondary particle are shown in each TXM image. Scale bar is  $10 \mu m$ .

The two-phase morphology observed in LFP secondary particles differs significantly from that in single-crystalline particles<sup>11,12</sup>. In microsized LFP crystallites, FP phase spreads rapidly and isotropically on the particle surface upon charging via a surface-reaction-limited growth mode<sup>12</sup>, and an LFP/FP coreshell geometry could readily develop at 20%-30% SOCs<sup>11</sup> without forming filamentary FP domains. Such difference points to the important role of the polycrystallinity of LFP particles.

On the other hand, the filamentary phase structure is in excellent agreement with a recent macroscopic analysis conducted by Xiang et al.<sup>26</sup>, who fitted the chronoamperometry data with the Johnson-Mehl-Avrami-Kolmogorov (JMAK) equation<sup>35</sup> to investigate the phase transformation kinetics in LiMn<sub>1-x</sub>Fe<sub>x</sub>PO<sub>4</sub> agglomerates. They found that the fitted Avrami exponent could only be interpreted if the LFP or FP phase exhibits 1D growth in secondary particles although the microscopic mechanism of the growth process could not be revealed by the analysis. Our observation provides a clear explanation to this behavior.

In search of the origins of the reaction heterogeneity in LFP secondary particles, we first rule out extrinsic factors such as the non-uniform contact between particles and conductive additives and electrolyte as a possible cause. LFP has low electronic conductivity and relies on carbon additives to transport electrons within the electrode. Non-uniform coverage of the additives on particle surface may lead to spatial variation in the reaction rate, but it cannot explain why the new phase develops the filamentary shape. Similarly, incomplete wetting of particles by the electrolyte is not likely to be responsible for the observed two-phase morphology, which should instead result from the intrinsic properties of LFP secondary particles.

To shed light on the experimental findings, we simulated the (de)lithiation process in polycrystalline LFP in 2D by employing a phase-field model <sup>20,36</sup> with the depth-averaging approximation <sup>37</sup> (see Methods). Individual grains in the system can exchange lithium and transmit stress with each other like in a consolidated secondary particle, and their crystallographic orientations are randomly distributed in the 3D orientation space. The model considers the 1D Li transport along the [010] axis in LFP, which results in variation in the in-plane diffusivity and Li surface (de)intercalation flux between grains due to their different orientations. Coherency stress, which arises from the lattice mismatch between LFP and FP phases, is also captured in the model.

Two sets of LFP's anisotropic properties potentially contribute to the 1D phase growth behavior in secondary particles. First, lithium can move fast along the [010] axis but has much lower diffusivity in other directions at room temperature<sup>39,40</sup>. It is possible that lithium (de)insertion occurs more facilely on primary particles whose [010] axis is aligned with the surface normal, resulting in non-uniform phase growth. Second, the lattice mismatch between LFP and FP is also strongly anisotropic, which is 5% along the [100] axis, 3.6% along [010] and -1.9% along [001]<sup>38</sup>. Coherency stress arising from the LFP/FP misfit strain during phase transition is shown to cause anisotropic phase growth to minimize the elastic energy in single crystalline LiFePO<sub>4</sub> <sup>20,36,41-44</sup>.

Our simulations well reproduce the experimental observations. Figure 5a shows a polycrystal consisting of 200 grains after being delithiated to SOC = 30% at a rate of 0.1C. An animation of the

corresponding simulation can be found in Supplementary Movie S1. Filamentary FP domains form via 1D growth in the simulation, which bears close resemblance to the experiments. Additional simulations using different polycrystalline configurations all show similar two-phase morphology (Supplementary Figure S9). For a more quantitative comparison, we performed filament tracing analysis on the simulated FP domains. As shown in Figure 5b and c, the average length-to-diameter ratio (6.6) and diameter (0.6 times of the average grain size) of the FP filaments agree very well with their values measured from the 3D XANES data. Though the simulations use a smaller primary particle sizes (32 nm on average) than in the experiment for computational efficiency, our numerical test shows that doubling the grain size yields similar filamentary geometry of the FP domains (see Supplementary Figure S10), which suggests that the salient features of the phase distribution in LFP secondary particles are independent of the primary particle size. We thus conclude that the phase-field model provides a reliable description of the phase transformation process in polycrystalline LFP.

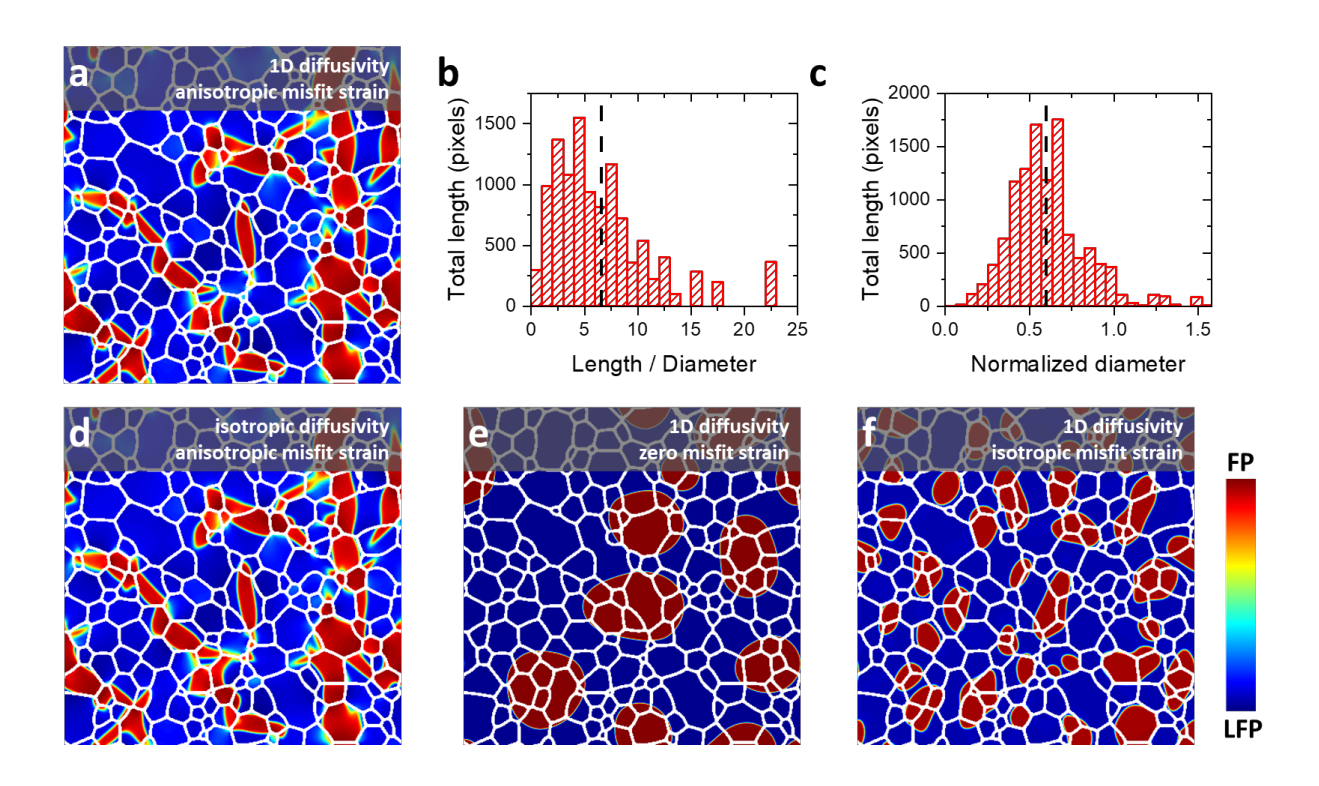


Figure 5. Phase-field simulation of phase evolution in polycrystalline LFP and the effects of 1D Li diffusivity and LFP/FP misfit strain on the two-phase morphology. a) Simulated two-phase structure in a 2D polycrystalline LFP (400 nm × 400 nm) charged to 30% SOC at 0.1C. Both anisotropic misfit strain

and 1D Li diffusivity are used in the simulation. White lines represent grain boundaries. **b**, **c**) Histograms of the FP filament length/diameter ratio and diameter (normalized by average grain size) at 30% SOC, respectively, which are obtained from filament tracing analysis of the aggregated results of six simulations. The black dashed lines in **b** and **c** represent the means. **d-f**) Two-phase structure from simulations that are similar to a) but assume **d**) isotropic Li diffusivity and anisotropic LFP/FP misfit strain, **e**) 1D Li diffusivity and no LFP/FP misfit strain, and **f**) 1D Li diffusivity and isotropic LFP/FP misfit strain (2.2%).

LFP is well known for its strongly anisotropic Li migration behavior at room temperature with fast Li diffusion along the [010] axis but much lower diffusivity in other directions<sup>39,40</sup>. It has been suggested in literature that the 1D Li diffusivity leads to 1D phase growth in LFP particles <sup>45,46</sup>. Using simulation, however, we demonstrate that the Li diffusion anisotropy is not a significant factor in controlling the reaction distribution in LFP polycrystals. This can be seen from the nearly identical phase distribution in Figure 5a and 5d, the latter of which is the same as the one for Figure 5a except that isotropic Li diffusivity is assumed.

While the 1D phase growth behavior does not depend on the 1D Li diffusivity, we confirmed that the (de)lithiation-induced coherency stress in the particles plays an important role. When coherency stress is removed from simulation by assuming no misfit strain between FP and LFP phases, FP phase grows isotropically in the polycrystal to span multiple grains in all directions and no longer possesses the filamentary morphology (Figure 5e). We also discovered that the anisotropy of the LFP/FP misfit strain is necessary for filamentary growth. When a hypothetic isomeric misfit strain of 2.2% (average of the lattice misfits along [100], [010] and [001]), FP domains do not display the filamentary morphology (Figure 5f), which is similar to the numerical observation in LFP single crystal that isotropic misfit leads to isotropic domain structure <sup>20</sup>.

We gained detailed insights from simulation on the nucleation and growth process of the new phase in polycrystalline LFP. Upon delithiation (or lithiation), FP (or LFP) phase first nucleates within grains that incur a low misfit strain energy because of their favorable orientations and geometries relative to the neighbor grains. Figure 6a presents a "transformation energy penalty" map for an LFP polycrystal, in which the transformation energy penalty  $\Delta E_{el}$  associated with a grain is calculated as the elastic energy generated

when this grain transforms into the FP phase alone. After charging to SOC = 10.8% at a rate of 0.1C, the initial FP nuclei (red regions) formed in the polycrystal reside in grains with the lowest  $\Delta E_{el}$ . After nucleation, FP domains preferentially grow along directions that are roughly normal to the [100] axis of the grains (Figure 6b). This is because LFP and FP phases have the largest lattice mismatch along [100] (5%), which favors the FP phase to extend in the orthogonal directions to reduce the misfit strain energy. Nevertheless, the angle between the FP filament growth direction and the [100] axis is not exactly 90° as illustrated in Figure 6b and 6c. This is consistent with the linear elasticity calculation by Cogswell and Bazant<sup>41</sup> of the habit plane between LFP and FP phases, which is the phase boundary orientation that minimizes the elastic energy. They find that the LFP/FP habit plane is at a small angle with the (100) plane due to the opposite signs of the LFP/FP misfit strains along [100] (5%) and [001] (-1.9%). Unlike single crystals, the misorientation between primary particles in the polycrystal imposes additional strain energy penalty on the thickening of an FP filament into the adjacent particles as its short axis is no longer perpendicular to the LFP/FP habit plane. This has the effect of confining the FP domain to within a single grain along the habit plane normal and results in the 1D growth phenomenon. Figure 6c shows that when the growth front of an FP domain reaches the grain boundary, it finds the path of "least resistance" into a neighbor grain by realigning its growth direction to within the local LFP/FP habit plane. The simulations reveal that the misfit stress exerts dominant influence on both the nucleation and growth steps of the phase transformation in polycrystalline LFP.

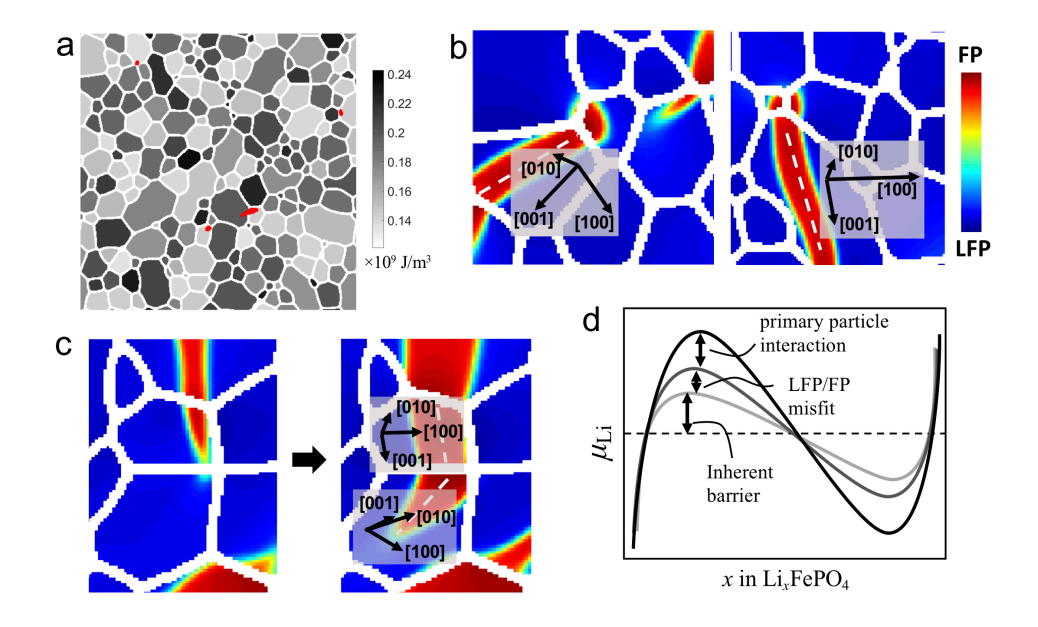


**Figure 6. Effect of misfit stress on the nucleation and growth in polycrystalline LFP. a)** Transformation energy penalty map of an LFP polycrystal ( $400 \times 400 \text{ nm}^2$ ) upon delithiation, in which the grayscale color of a grain represents the average misfit strain energy density generated by the transformation of this grain only into the FP phase. FP domains (red regions) formed upon charging to 10.8% SOC at 0.1C are superimposed onto the map. **b)** Illustration of two FP filaments relative to the local grain orientation. **c)** Illustration of an FP filament changing its growth direction when propagating into another grain. The angles between the growth direction of the four filament segments (white dashed lines) and the local [100] axis in **b** and **c** are 79° (**b**, left), 71° (**b**, right), 78° (**c**, top) and 74° (**c**, bottom), respectively. **d)** Schematic of the transformation barrier for lithium intercalation in LFP and how it is affected by the LFP/FP misfit and secondary particle structure.

Our simulations also corroborate the experimental observation that the reaction distribution in LFP secondary particles is insensitive to (dis)charging rate. Supplementary Figure S11 shows the two-phase structures in an LFP polycrystal when it is delithiated or lithiated to SOC = 50% at different rates. They are very similar to each other and symmetric between charging and discharging. Notably, Li (de)intercalation is not uniform among the grains even at 10C. At any given time in all the simulations, only a small fraction of grains actively (de)intercalate Li in the system, which resembles the "particle-to-particle" intercalation behavior observed in dispersed LFP nanoparticle ensemble<sup>25</sup>. However, a notable difference between the two types of systems is that the active particle fraction in the latter increases with lithiation rate, leading to a transition to concurrent Li intercalation at sufficiently high rates<sup>25</sup>, which is nonetheless not seen in the simulations of polycrystalline LFP.

The different rate dependence of the reaction heterogeneity in aggregated vs dispersed LFP nanoparticles could be explained by considering the energy barrier associated with the phase transformation process. For LFP and phase-separating electrode materials in general, particle-to-particle intercalation results from an intrinsic transformation energy barrier <sup>25</sup>, which is manifested by local maxima in the Li chemical potential as a function of Li concentration (Figure 6d). Concurrent intercalation only occurs when the applied overpotential is significantly larger than this barrier so that all the particles are activated. When there is lattice mismatch between the lithiated and delithiated phases as in the case of LFP, the transformation barrier is enhanced by the misfit strain energy. Compared to dispersed LFP nanoparticles, primary particles in agglomerates experience an even larger strain energy penalty upon transformation due to the volume constraints imposed by neighbor particles, which further increases the barrier that requires a higher overpotential or current to overcome. When the grains are separated from each other to remove the misfit stress between them in our polycrystal simulation, the system indeed switches to concurrent Li intercalation at 5C discharging (Supplementary Figure S12). The contrast clearly demonstrates that the strong elastic interaction between primary particles in polycrystalline LFP reduces the fraction of active primary particles and makes it more difficult to achieve uniform Li (de)intercalation on particle surface. It also shows that the intergranular stress contributes to both the inter- and intra-primary-particle heterogeneities observed in the experiment, and its elimination could improve the uniformity at both scales especially at high rates.

To mitigate reaction heterogeneity in LFP secondary particles and its detrimental effects, our study suggests that the intentional inclusion of some degrees of internal porosity would be advantageous as it reduces the intergranular elastic interaction that would increase the active fraction of primary particles during the (dis)charging process. In addition, it is recently demonstrated that aligning the (003) planes of NMC primary particles with the radial direction of secondary particles improves reaction uniformity by shortening Li diffusion distance<sup>4</sup>, which leads to lower cell polarization, better capacity retention and enhanced rate performance. Due to LFP's highly anisotropic properties, similar strategies of tailoring the

primary particle orientation are also applicable to LFP secondary particles. For instance, aligning the [100] axis of a primary particle with the [001] axis of its neighbor particles and vice versa would effectively lower the internal stress because the volume change of the particle upon cycling could be better accommodated by its surrounding thanks to the opposite signs of the LFP/FP lattice mismatch along [100] (5%) and [001] (-1.9%). The rational design of the agglomerate microstructure, which has not yet been widely explored, will benefit from a mechanistic understanding of the reaction heterogeneity at this scale. Nevertheless, maximizing battery performance also requires engineering structures across length scales. As an example, to maintain the same energy density, introducing internal porosity in secondary particles necessitates a decrease in the inter-particle porosity, which impedes electrolyte transport and enhances the reaction polarization across the electrode. Careful optimization of the porosity distribution at the intra- vs interagglomerate levels is needed to improve the overall reaction uniformity of battery cells.

In conclusion, reaction distribution in LFP secondary particles was investigated by 3D and operando 2D XANES imaging in combination with phase-field simulations. Upon delithiation (lithiation), the FP (LFP) phase exhibits 1D growth behavior in secondary particles and forms rate-independent filament-like domains with the average diameter smaller than the primary particle size, which can be attributed to the effect of coherency stress from the LFP/FP lattice misfit instead of the 1D Li diffusivity. Due to strong elastic interaction, nanoscale primary particles in LFP secondary particles experience more pronounced reaction heterogeneity than dispersed nanoparticles, and Li (de)intercalation will remain non-uniform on the secondary particle surface at high (dis)charging rates.

#### Acknowledgments

F.W. and M.T. were supported by the Department of Energy, Basic Energy Sciences under project DE-SC0019111. K.Y. acknowledges support from the National Science Foundation under project CMMI-1929949. 3D XANES experiments were performed at beamline 18-ID, National Synchrotron Light Source II, Brookhaven National Laboratory, which are supported by the U.S. DOE, Office of Science, Office of Basic Energy Sciences under Contract No. DE-AC02-98CH10886. Use of the Advanced Photon Source,

an Office of Science User Facility operated for the U.S. DOE, Office of Science by Argonne National Laboratory, was supported by the U.S. DOE under Contract No. DE-AC02-06CH11357. Simulations were performed on supercomputers at the Texas Advanced Computing Center (TACC) at The University of Texas and the National Energy Research Scientific Computing Center, a DOE Office of Science User Facility supported by the Office of Science of the U.S. Department of Energy under Contract No. DE-AC02-05CH11231.

Supporting Information Available: Additional experimental and modeling methods and details, including 3D and 2D XANES images and phase-field simulations.

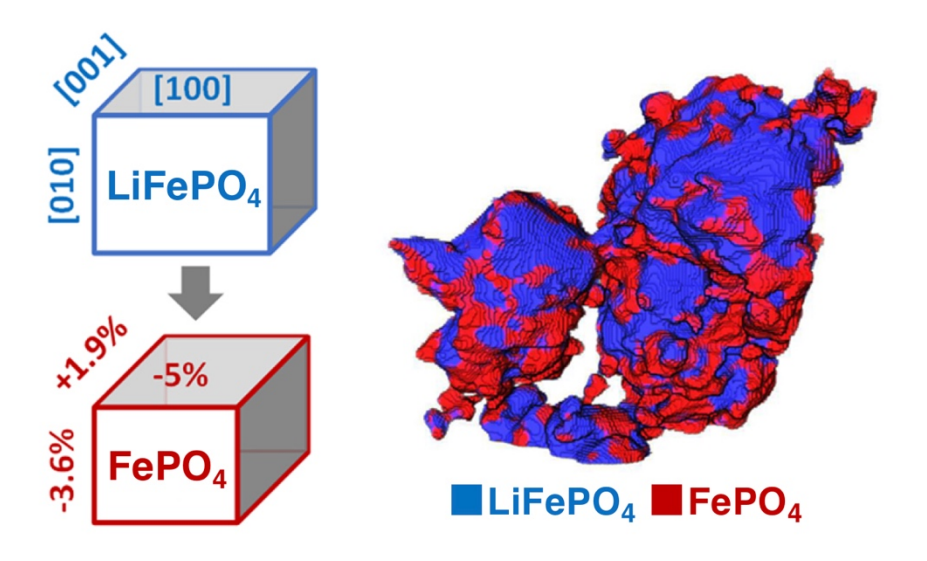
## Reference

- 1. Zhang, Y. X., Yang, Z. J., Tian, C. X. Probing and Quantifying Cathode Charge Heterogeneity in Li Ion Batteries. *Journal of Materials Chemistry A* 7, 23628 (2019).
- 2. Wang, F., Tang, M. A Quantitative Analytical Model for Predicting and Optimizing the Rate Performance of Battery Cells. *Cell Reports Physical Science* **1**, 100192 (2020).
- 3. Wang, F., Tang, M. Thermodynamic Origin of Reaction Non-Uniformity in Porous Battery Electrodes and Its Mitigation. *Journal of The Electrochemical Society* **167**, 120543 (2020).
- 4. Xu, Z. R., Jiang, Z. S., Kuai, C. G., Xu, R., Qin, C. D., Zhang, Y., Rahman, M. M., Wei, C. X., Nordlund, D., Sun, C. J., Xiao, X. H., Du, X. W., Zhao, K. J., Yan, P. F., Liu, Y. J., Lin, F. Charge Distribution Guided by Grain Crystallographic Orientations in Polycrystalline Battery Materials. *Nature Communications* 11, 1 (2020).
- 5. Chen, K. H., Goel, V., Namkoong, M. J., Wied, M., Muller, S., Wood, V., Sakamoto, J., Thornton, K., Dasgupta, N. P. Enabling 6C Fast Charging of Li-Ion Batteries with Graphite/Hard Carbon Hybrid Anodes. *Advanced Energy Materials* 11, 2003336 (2021).
- 6. Liu, J., Kunz, M., Chen, K., Tamura, N., Richardson, T. J. Visualization of Charge Distribution in a Lithium Battery Electrode. *Journal of Physical Chemistry Letters* **1**, 2120 (2010).
- 7. Liu, H., Kazemiabnavi, S., Grenier, A., Vaughan, G., Di Michiel, M., Polzin, B. J., Thornton, K., Chapman, K. W., Chupas, P. J. Quantifying Reaction and Rate Heterogeneity in Battery Electrodes in 3D through Operando X-ray Diffraction Computed Tomography. *ACS Appl. Mater. Inter.* 11, 18386 (2019).
- 8. Yang, Y., Xu, R., Zhang, K., Lee, S. J., Mu, L. Q., Liu, P. F., Waters, C. K., Spence, S., Xu, Z. R., Wei, C. X., Kautz, D. J., Yuan, Q. X., Dong, Y. H., Yu, Y. S., Xiao, X. H., Lee, H. K., Pianetta, P., Cloetens, P., Lee, J. S., Zhao, K. J., Lin, F., Liu, Y. J. Quantification of Heterogeneous Degradation in Li-Ion Batteries. *Advanced Energy Materials* **9**, 1900674 (2019).
- 9. Nanda, J., Remillard, J., O'Neill, A., Bernardi, D., Ro, T., Nietering, K. E., Go, J. Y., Miller, T. J. Local State-of-Charge Mapping of Lithium-Ion Battery Electrodes. *Advanced Functional Materials* **21**, 3282 (2011).
- 10. Nowack, L., Grolimund, D., Samson, V., Marone, F., Wood, V. Rapid Mapping of Lithiation Dynamics in Transition Metal Oxide Particles with Operando X-ray Absorption Spectroscopy. *Sci. Rep.* **6**, 21479 (2016).
- 11. Wang, J., Karen Chen-Wiegart, Y. C., Eng, C., Shen, Q., Wang, J. Visualization of Anisotropic-Isotropic Phase Transformation Dynamics in Battery Electrode Particles. *Nature Communications* 7, 12372 (2016).
- 12. Hong, L., Li, L., Chen-Wiegart, Y. C., Wang, J., Xiang, K., Gan, L., Li, W., Meng, F., Wang, F., Wang, J., Chiang, Y.-M., Jin, S., Tang, M. 2D Li Diffusion Behavior and Probable Hybrid Phase Transformation Kinetics in Olivine Lithium Iron Phosphate. *Nature Communications* **8**, 1194 (2017).
- 13. Gent, W. E., Li, Y., Ahn, S., Lim, J., Liu, Y., Wise, A. M., Gopal, C. B., Mueller, D. N., Davis, R., Weker, J. N., Park, J. H., Doo, S. K., Chueh, W. C. Persistent State-of-Charge Heterogeneity in Relaxed, Partially Charged Li<sub>1-x</sub>Ni<sub>1/3</sub>Co<sub>1/3</sub>Mn<sub>1/3</sub>O<sub>2</sub> Secondary Particles. *Adv. Mater.* **28**, 6631 (2016).
- 14. Tian, C. X., Xu, Y. H., Nordlund, D., Lin, F., Liu, J., Sun, Z. H., Liu, Y. J., Doeff, M. Charge Heterogeneity and Surface Chemistry in Polycrystalline Cathode Materials. *Joule* **2**, 464 (2018).
- 15. Yao, K. P. C., Okasinski, J. S., Kalaga, K., Shkrob, I. A., Abraham, D. P. Quantifying Lithium Concentration Gradients in The Graphite Electrode of Li-Ion Cells Using Operando Energy Dispersive X-Ray Diffraction. *Energy & Environmental Science* **12**, 656 (2019).
- 16. Yu, Y. S., Farmand, M., Kim, C., Liu, Y. J., Grey, C. P., Strobridge, F. C., Tyliszczak, T., Celestre, R., Denes, P., Joseph, J., Krishnan, H., Maia, F. R. N. C., Kilcoyne, A. L. D., Marchesini, S., Leite, T. P. C., Warwick, T., Padmore, H., Cabana, J., Shapiro, D. A. Three-

- Dimensional Localization of Nanoscale Battery Reactions Using Soft X-Ray Tomography. *Nature Communications* **9**, 921 (2018).
- 17. Danner, T., Singh, M., Hein, S., Kaiser, J., Hahn, H., Latz, A. Thick Electrodes for Li-Ion Batteries: A Model Based Analysis. *Journal of Power Sources* **334**, 191 (2016).
- 18. Li, Y., Weker, J. N., Gent, W. E., Mueller, D. N., Lim, J., Cogswell, D. A., Tyliszczak, T., Chueh, W. C. Dichotomy in the Lithiation Pathway of Ellipsoidal and Platelet LiFePO<sub>4</sub> Particles Revealed through Nanoscale Operando State-of-Charge Imaging. *Advanced Functional Materials* **25**, 3677 (2015).
- 19. Kuppan, S., Xu, Y., Liu, Y., Chen, G. Phase Transformation Mechanism in Lithium Manganese Nickel Oxide Revealed by Single-Crystal Hard X-Ray Microscopy. *Nature Communications* **8**, 14309 (2017).
- 20. Yang, K. Q., Tang, M. Three-Dimensional Phase Evolution and Stress-Induced Non-Uniform Li Intercalation Behavior in Lithium Iron Phosphate. *Journal of Materials Chemistry A* **8**, 3060 (2020).
- 21. Zhang, Y. T., Tang, M. Stress-Induced Intercalation Instability. *Acta Materialia* **201**, 158 (2020).
- 22. Lim, J., Li, Y. Y., Alsem, D. H., So, H., Lee, S. C., Bai, P., Cogswell, D. A., Liu, X. Z., Jin, N., Yu, Y. S., Salmon, N. J., Shapiro, D. A., Bazant, M. Z., Tyliszczak, T., Chueh, W. C. Origin and Hysteresis of Lithium Compositional Spatiodynamics Within Battery Primary Particles. *Science* **353**, 566 (2016).
- 23. Bazant, M. Z. Thermodynamic Stability Of Driven Open Systems and Control of Phase Separation by Electro-Autocatalysis. *Faraday Discussions* **199**, 423 (2017).
- 24. Delmas, C., Maccario, M., Croguennec, L., Le Cras, F., Weill, F. Lithium Deintercalation in LiFePO<sub>4</sub> Nanoparticles via A Domino-Cascade Model. *Nature Materials* 7, 665 (2008).
- 25. Li, Y., El Gabaly, F., Ferguson, T. R., Smith, R. B., Bartelt, N. C., Sugar, J. D., Fenton, K. R., Cogswell, D. A., Kilcoyne, A. L., Tyliszczak, T., Bazant, M. Z., Chueh, W. C. Current-Induced Transition from Particle-by-Particle to Concurrent Intercalation In Phase-Separating Battery Electrodes. *Nature Materials* 13, 1149 (2014).
- 26. Xiang, K., Yang, K. Q., Carter, W. C., Tang, M., Chiang, Y. M. Mesoscopic Phase Transition Kinetics in Secondary Particles of Electrode-Active Materials in Lithium-Ion Batteries. *Chemistry of Materials* **30**, 4216 (2018).
- Wang, J., Chen-Wiegart, Y. C., Wang, J. In Operando Tracking Phase Transformation Evolution of Lithium Iron Phosphate with Hard X-Ray Microscopy. *Nature Communications* **5**, 4570 (2014).
- 28. Li, L., Chen-Wiegart, Y. C., Wang, J., Gao, P., Ding, Q., Yu, Y. S., Wang, F., Cabana, J., Wang, J., Jin, S. Visualization of Electrochemically Driven Solid-State Phase Transformations Using Operando Hard X-Ray Spectro-Imaging. *Nature Communications* **6**, 6883 (2015).
- 29. Wang, J., Eng, C., Chen-Wiegart, Y. C., Wang, J. Probing Three-Dimensional Sodiation-Desodiation Equilibrium In Sodium-Ion Batteries by In situ Hard X-Ray Nanotomography. *Nature Communications* **6**, 7496 (2015).
- 30. Wei, C. X., Xia, S. H., Huang, H., Mao, Y. W., Pianetta, P., Liu, Y. J. Mesoscale Battery Science: The Behavior of Electrode Particles Caught on a Multispectral X-ray Camera. *Accounts Chem. Res.* **51**, 2484 (2018).
- 31. Xu, Y., Hu, E., Zhang, K., Wang, X., Borzenets, V., Sun, Z., Pianetta, P., Yu, X., Liu, Y., Yang, X.-Q., Li, H. In situ Visualization of State-of-Charge Heterogeneity within a LiCoO<sub>2</sub> Particle that Evolves upon Cycling at Different Rates. *ACS Energy Lett* **2**, 1240 (2017).
- 32. Thermo Fisher Scientific Avizo 2019. <a href="https://assets.thermofisher.com/TFS-Assets/MSD/Product-Guides/users-guide-avizo-software-2019.pdf">https://assets.thermofisher.com/TFS-Assets/MSD/Product-Guides/users-guide-avizo-software-2019.pdf</a>
- 33. Weber, B., Greenan, G., Prohaska, S., Baum, D., Hege, H. C., Muller-Reichert, T., Hyman, A. A., Verbavatz, J. M. Automated Tracing of Microtubules in Electron Tomograms of Plastic Embedded Samples of Caenorhabditis Elegans Embryos. *J. Struct. Biol.* **178**, 129 (2012).

- 34. Li, Y. Y., Chen, H. R., Lim, K., Deng, H. D., Lim, J., Fraggedakis, D., Attia, P. M., Lee, S. C., Jin, N., Moskon, J., Guan, Z. X., Gent, W. E., Hong, J., Yu, Y. S., Gaberscek, M., Islam, M. S., Bazant, M. Z., Chueh, W. C. Fluid-Enhanced Surface Diffusion Controls Intraparticle Phase Transformations. *Nature Materials* 17, 915 (2018).
- 35. Johnson, W. A., Mehl, R. F. Reaction kinetics in processes of nucleation and growth. *Transations of A.I.M.E.* **135**, 416 (1939).
- 36. Tang, M., Belak, J. F., Dorr, M. R. Anisotropic Phase Boundary Morphology in Nanoscale Olivine Electrode Particles. *J. Phys. Chem. C* **115**, 4922 (2011).
- 37. Singh, G. K., Ceder, G., Bazant, M. Z. Intercalation Dynamics In Rechargeable Battery Materials: General Theory and Phase-Transformation Waves In LiFePO<sub>4</sub>. *Electrochimica Acta* **53**, 7599 (2008).
- 38. Meethong, N., Huang, H. Y. S., Speakman, S. A., Carter, W. C., Chiang, Y. M. Strain Accommodation during Phase Transformations in Olivine-Based Cathodes as a Materials Selection Criterion for High-Power Rechargeable Batteries. *Advanced Functional Materials* 17, 1115 (2007).
- 39. Morgan, D., Van der Ven, A., Ceder, G. Li Conductivity in  $Li_xMPO_4$  (M = Mn, Fe, Co, Ni) Olivine Materials. *Electrochemical and Solid-State Letters* 7, A30 (2004).
- 40. Nishimura, S., Kobayashi, G., Ohoyama, K., Kanno, R., Yashima, M., Yamada, A. Experimental Visualization of Lithium Diffusion in Li<sub>x</sub>FePO<sub>4</sub>. *Nature Materials* **7**, 707 (2008).
- 41. Cogswell, D. A., Bazant, M. Z. Coherency Strain And The Kinetics Of Phase Separation in LiFePO<sub>4</sub> Nanoparticles. *ACS Nano* **6**, 2215 (2012).
- 42. Cogswell, D. A., Bazant, M. Z. Size-Dependent Phase Morphologies in LiFePO<sub>4</sub> Battery Particles. *Electrochemistry Communications* **95**, 33 (2018).
- 43. Heo, T. W., Tang, M., Chen, L. Q., Wood, B. C. Defects, Entropy, and the Stabilization of Alternative Phase Boundary Orientations in Battery Electrode Particles. *Advanced Energy Materials* **6**, 1501759 (2016).
- 44. Yang, K. Q., Tang, M. Three-Dimensional Phase Evolution and Stress-Induced Non-Uniform Lithium Intercalation Behavior in Lithium Iron Phosphate. *Journal of Materials Chemistry A* **8**, 3060 (2019).
- 45. Allen, J. L., Jow, T. R., Wolfenstine, J. Kinetic Study of the Electrochemical FePO<sub>4</sub> to LiFePO<sub>4</sub> Phase Transition. *Chemistry of Materials* **19**, 2108 (2007).
- 46. Oyama, G., Yamada, Y., Natsui, R., Nishimura, S., Yamada, A. Kinetics of Nucleation and Growth in Two-Phase Electrochemical Reaction of Li<sub>x</sub>FePO<sub>4</sub>. *Journal of Physical Chemistry C* **116**, 7306 (2012).

ToC Graphic



# **Supplementary Materials for**

# Reaction Heterogeneity in LiFePO<sub>4</sub> Agglomerates and the Role of Intercalation-Induced Stress

Fan Wang<sup>1†</sup>, Kaiqi Yang<sup>1†</sup>, Mingyuan Ge<sup>2</sup>, Jiajun Wang<sup>2,3</sup>, Jun Wang<sup>2</sup>, Xianghui Xiao<sup>2</sup>, Wah-Keat Lee<sup>2</sup>, Linsen Li<sup>4</sup>, Ming Tang<sup>1\*</sup>

- Department of Materials Science & NanoEngineering, Rice University, Houston, TX 77005, USA
- National Synchrotron Light Source II, Brookhaven National Laboratory, Upton, NY 11973,
   USA
- School of Chemistry and Chemical Engineering, Harbin Institute of Technology, 150001,
   Harbin, China
- 4. Department of Chemical Engineering, Shanghai Electrochemical Energy Device Research Center (SEED), Shanghai Jiao Tong University, Shanghai, 200240, China

<sup>&</sup>lt;sup>†</sup> These authors contribute equally.

<sup>\*</sup>Corresponding author email: mingtang@rice.edu

#### Methods

## Sample preparation

To prepare the electrodes for the TXM-XANES measurement, commercial LiFePO<sub>4</sub> powder (BTR), carbon black (Super P, Timcal) and polyvinylidene fluoride (Kynar HSV1800, Arkema) in a weight ratio of 50:25:25 were mixed with N-Methyl-2-Pyrrolidone (NMP) into a slurry and coated on carbon paper (Toray). The electrode was dried in an air convection oven at 110°C for ~12h. CR2032-type coin cells were assembled with 12 mm-diameter LiFePO<sub>4</sub> electrode discs, Celgard 2500 separators and Li metal discs as anode in an argon-filled glovebox (O<sub>2</sub> / H<sub>2</sub>O level < 1ppm). The electrolyte used was 1 M LiPF<sub>6</sub> in 1:1 (v/v) mixture of ethylene carbonate (EC) and diethyl carbonate (DEC) with 10% of fluoroethylene carbonate (FEC) as additive (LBC3401A4, Capchem). Before further testing, all cells were pre-cycled at 0.1C (1C = 170 mA/g) for 3 times to reach a stable capacity of ~170 mAh g<sup>-1</sup> between 2.5 V and 4.2 V. After charged/discharged to the desired SOCs, the LiFePO<sub>4</sub> electrodes for ex-situ 3D XANES measurement were disassembled from the coin cells within 5 minutes, washed in dimethyl carbonate (DMC) for multiple times and dried in the Ar-filled glovebox to prevent lithium redistribution within the electrodes. Prior to the TXM-XANES experiments, the electrodes were sealed by two Kapton films to protect the active material against oxygen and moisture in the air.

#### Characterization

The morphology of LiFePO<sub>4</sub> secondary particles was studied by a FEI Quanta 400 scanning electron microscope (SEM) with an accelerating voltage at 15 keV. Ex-situ 3D XANES imaging was performed at the Full-Field X-ray Imaging (FXI, 18-ID) beamline at the National Synchrotron Light Source II (NSLS-II), Brookhaven National Laboratory. Nano-tomography datasets of LiFePO<sub>4</sub> samples were collected at 71 energies, which have an interval of 1 eV near the Fe K-edge (7112 eV), 10 eV in the pre-edge region and 40 eV in the post-edge region. Each dataset was collected in the fly scan mode with a sample rotation speed of 4 deg/s, exposure time of 0.025 s and 2×2 camera binning, which result in a spatial resolution of 40 nm.

Tomographic images were reconstructed and aligned using the Python package PyXAS <sup>1</sup>. The pore phase in the secondary particles was identified based on the absorption contrast of the tomographic images and the internal porosity was calculated accordingly. In-situ operando 2D XANES imaging was conducted at beamline X8C, Advanced Photo Sources using a perforated CR-2032 coin cell. The holes on the positive and negative cases were sealed by Kapton tapes. 2D FF-TXM images were collected across the Fe K-edge from 7091 to 7285 eV with a 2 eV step size. The XANES spectra at each voxel or pixel were fitted by the reference spectra of LiFePO<sub>4</sub> and FePO<sub>4</sub> to determine the local phase fraction. Visualization of the 3D phase distribution in LiFePO<sub>4</sub> particles and the filament tracing analysis were carried out in Avizo 9.0®. In the filament tracing analysis, FP (or LFP) domains in a secondary particle are approximated by (interconnected) tubes. The centerlines of the tubes are determined by skeletonizing the domains, which produces a spatial graph, and the tube diameters are calculated from the volume of the domain segments.

### Phase field simulation

The Voronoi tessellation (V-T) method is used to generate 2D periodic polycrystalline configurations, which are relaxed by grain growth simulations <sup>2</sup> to remove structural artifacts known to V-S-generated polycrystals and keep the number of grains around 200. Each grain is assigned a random crystallographic orientation in the 3D orientation space.

We use a previously reported phase-field model  $^{3,4}$  to simulate the (dis)charging process in LFP polycrystals. In the model, the Li site occupancy fraction c (0<c<1) serves as the order parameter to both represent the Li concentration distribution and distinguish between the LFP (c=1) and FP (c=0) phases. The free energy of the system is expressed as

$$F = \int_{V} \left[ f_{\text{chem}}(c) + f_{\text{el}}(\epsilon_{ij}, c) + \frac{\kappa}{2} (\nabla c)^{2} \right] dV$$
 1)

where  $f_{\text{chem}}$  is the stress-free homogeneous free energy density of LFP, which is described by a regular solution model,

$$f_{\text{chem}} = \{RT[c \ln c + (1-c) \ln(1-c)] + \Omega c (1-c)]\} / V_m$$
 2)

where  $\Omega = 12$  kJ/mol is the regular solution coefficient that characterizes LFP's phase separation behavior,  $V_m = 43.8$  cm<sup>3</sup>/mol is LFP's molar volume, R is the gas constant and T = 298 K.  $f_{el}$  is the linear elastic energy density:

$$f_{\rm el} = \frac{1}{2} C_{ijkl} (\epsilon_{ij} - \epsilon_{ij}^0 c) (\epsilon_{kl} - \epsilon_{kl}^0 c)$$
3)

where the Einstein summation convention is used.  $\epsilon_{ij} = (\partial u_j/\partial x_i + \partial u_i/\partial x_j)/2$  is the small strain tensor and  $u_i$  is the displacement vector. The Vegard's law is assumed here for the Li-concentration-dependent transformation strain. In the crystal coordinate system, the misfit strain tensor between stoichiometric LFP and FP is  $\epsilon_{11}^0 = 5\%$  ([100] axis),  $\epsilon_{22}^0 = 3.6\%$  ([010]),  $\epsilon_{33}^0 = -1.9\%$  ([001]) and  $\epsilon_{ij}^0 = 0$  ( $i \neq j$ ) <sup>5</sup>.  $C_{ijkl}$  is taken as the average of LiFePO<sub>4</sub> and FePO<sub>4</sub> stiffness tensors from DFT calculations <sup>6</sup>. The gradient energy coefficient  $\kappa$  in Eq. 1 is set as  $1.68 \times 10^{-12}$  J cm<sup>-1</sup>. It is chosen to produce the average of the (100), (010) and (001) LFP/FP interface energies from first-principles calculations <sup>7</sup>. Using calculus of variation, the Li chemical potential is derived from Eq. 1 to be:

$$\mu_{\text{Li}} = \frac{\delta F}{\delta c} = \frac{\partial f_{chem}}{\partial c} - C_{ijkl} \epsilon_{ij}^{0} (\epsilon_{kl} - \epsilon_{kl}^{0} c) - \kappa \nabla^{2} c$$

$$(4)$$

Depth-averaging approximation <sup>8-10</sup> is employed to simplify the simulations to 2D. The Li concentration is assumed to be uniform in the depth direction of the system (z axis). Its evolution within the x-y plane of the system is governed by the Cahn-Hilliard dynamics<sup>11,12</sup>

$$\frac{\partial c}{\partial t} = \nabla \cdot \left[ \mathbf{M} c (1 - c) \mu_{\text{Li}} \right] + \frac{j_{\text{Li}}}{L}$$
 5)

where the Li mobility tensor **M** is related to the Li diffusivity as  $M_{ij} = D_{ij}V_m/RT$ . DFT calculations<sup>13</sup> show that Li diffusion in LFP is fast along [010] and much slower in the [100] and [010] directions. In simulations, we set  $D_{[010]} = 10^{-12}$  cm<sup>2</sup> s<sup>-1</sup> <sup>14</sup> and  $D_{[100]}$  and  $D_{[001]}$  to be 1% of the  $D_{[010]}$  value. Because each grain in the polycrystal has a different orientation, the Li diffusivity  $(D_{ij})$ , misfit strain  $(\epsilon_{ij}^0)$  and elastic moduli  $(C_{ijkl})$  tensors are spatially dependent. Their values are calculated from the local crystallographic orientation using the tensor transformation rule.

In Eq. 5,  $j_{Li}$  is the Li surface flux entering the system in the z direction and described by the Butler-Volmer equation

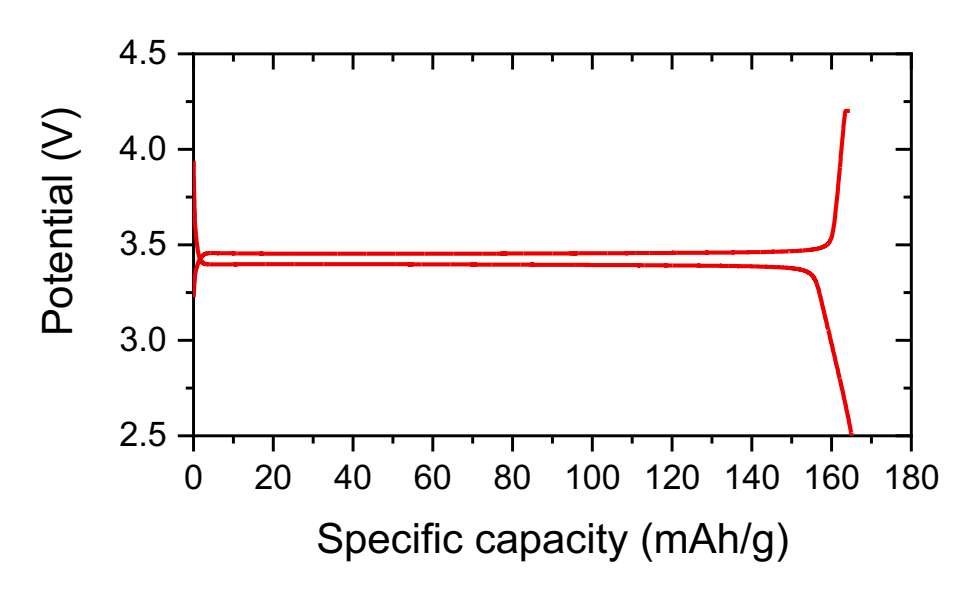
$$j_{\text{Li}} = \frac{v_{\text{m}}}{F} \left| \cos \theta_z \right| j_0 \left[ \exp \left( \frac{\left( \mu_{\text{Li}}^{\text{electrolyte}} - \mu_{\text{Li}} \right)}{2RT/V_{\text{m}}} \right) - \exp \left( - \frac{\left( \mu_{\text{Li}}^{\text{electrolyte}} - \mu_{\text{Li}} \right)}{2RT/V_{\text{m}}} \right) \right]$$
 6)

where F is the Faraday constant,  $j_0$  is the exchange current density and set to 0.01 A m<sup>-2</sup> <sup>15</sup>, and  $\mu_{Li}^{electrolyte}$  is the Li chemical potential of lithium in electrolyte. Because of the 1D Li diffusion behavior, the surface insertion flux is assumed to be proportional to the areal density of [010] Li migration channels on the system surface, which scales with  $|cos\theta_z|$  with  $\theta_z$  being the angle between the [010] axis of the grain and the z axis. When simulating the (dis)charging process under the constant current condition,  $\mu_{Li}^{electrolyte}$  is adjusted at each time step to produce a fixed total Li (de)insertion flux specified by the given C rate.

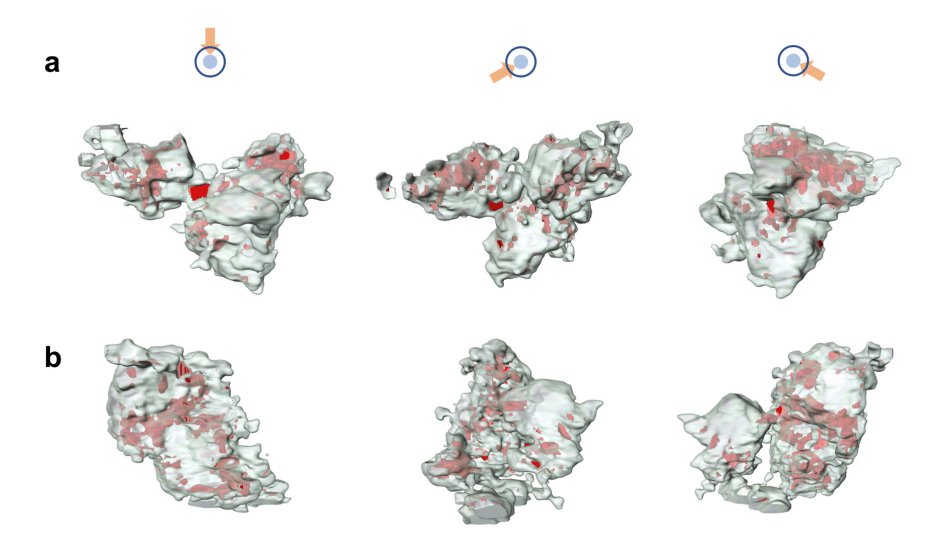
Eq. 5 and 6 are solved in conjunction with the mechanical equilibrium equation of the linear elasticity theory:

$$\frac{\partial \sigma_{ij}}{\partial x_i} = \frac{\partial}{\partial x_i} \left[ C_{ijkl} \left( \epsilon_{kl} - \epsilon_{kl}^0 c \right) \right] = 0 \tag{7}$$

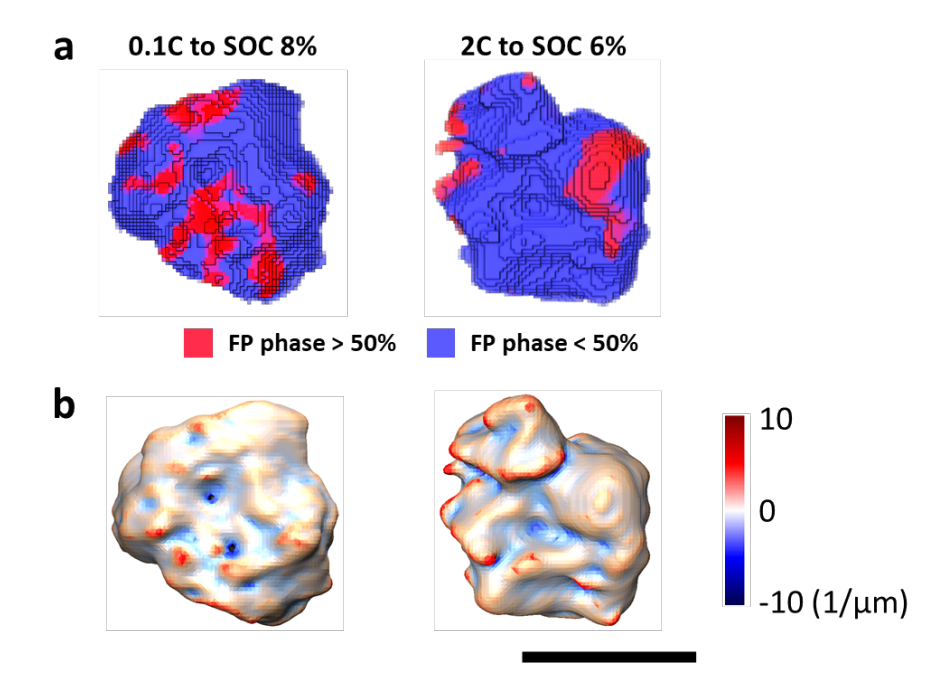
Grain boundaries are assumed to be coherent in stress calculation. Periodic boundary conditions are applied to Li concentration, stress and strain variables within the *x-y* plane. Simulations are performed in COMSOL Multiphysics® 5.3a.



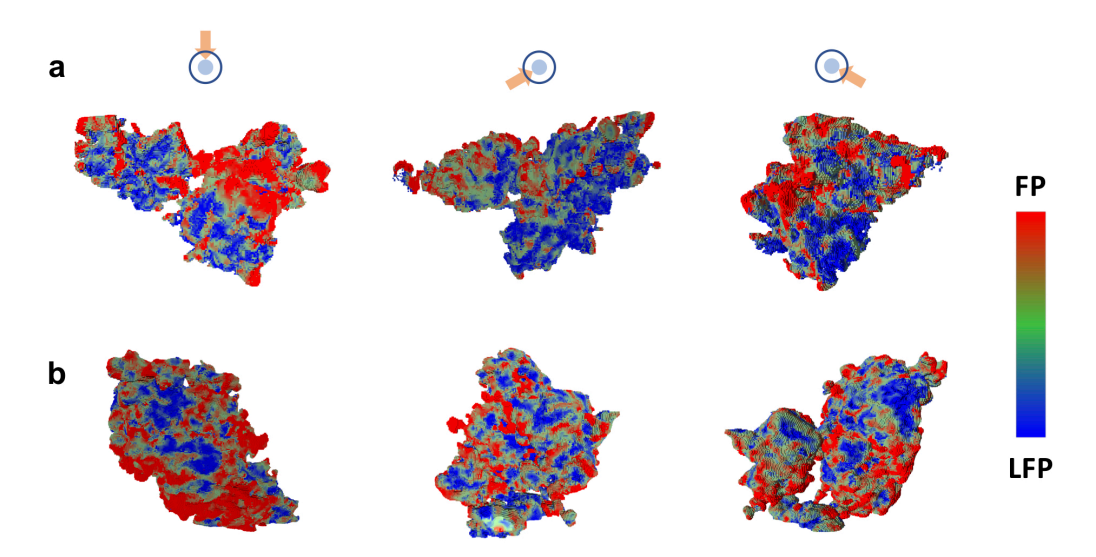
Supplementary Figure S1. Potential profile of the LFP secondary particles used in this study when cycled at  $0.1\mathrm{C}$ .



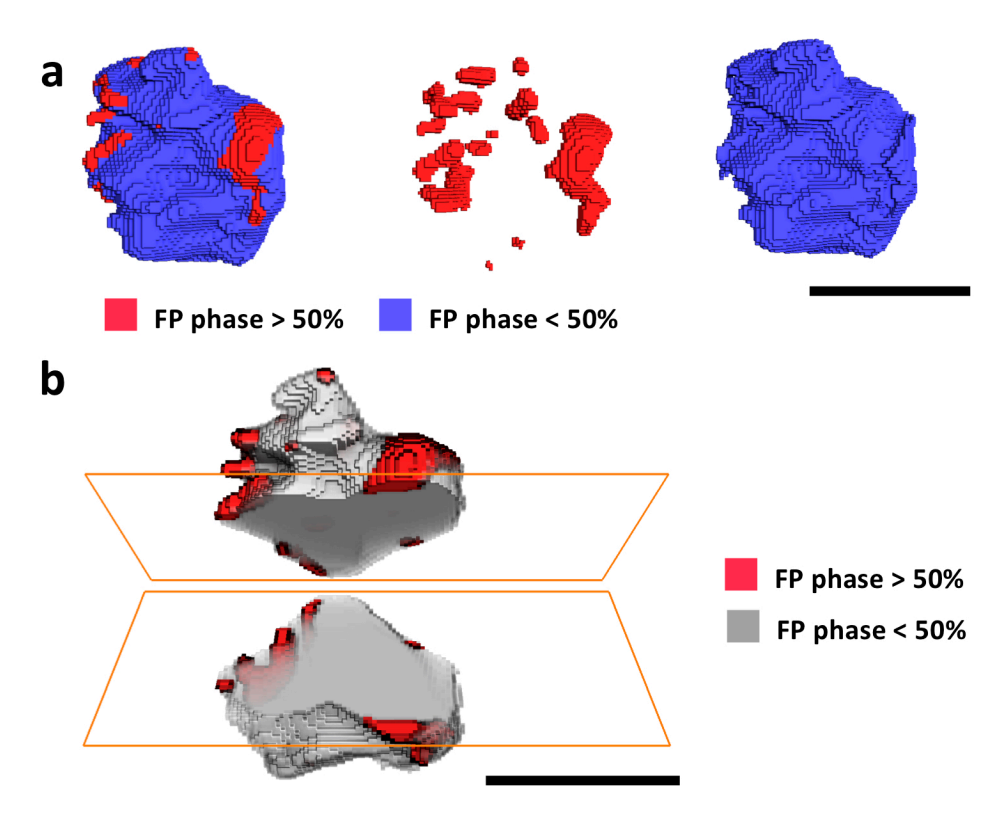
**Supplementary Figure S2. Pore phase within LFP secondary particles.** The pore phase in the secondary particles shown in Figure 2a and 2b is visualized as the red region in **a)** and **b)**, respectively. The internal porosity, calculated as the ratio between the pore and total particle volumes, the is 3.4% and 4.2% for the particles in **a)** and **b)**, respectively.



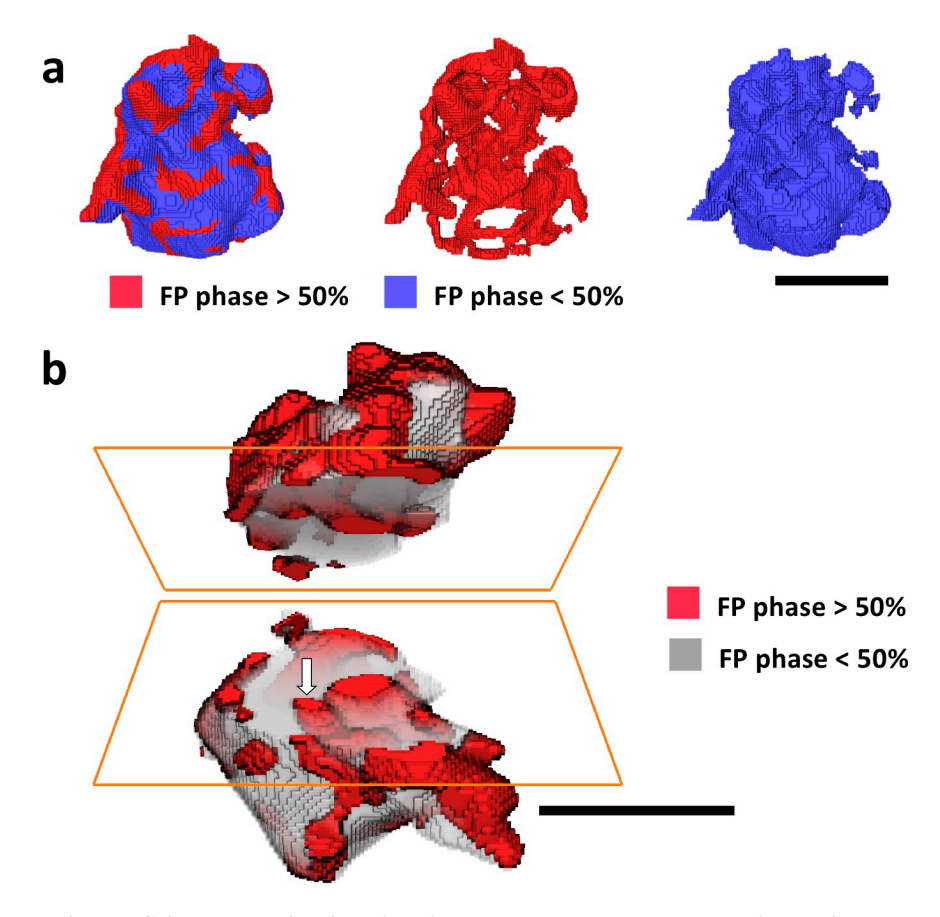
Supplementary Figure S3. a) Phase distribution and b) mean surface curvature mapping of two partially delithiated secondary particles charged at 0.1C and 2C, respectively. Scale bar is 2  $\mu$ m.



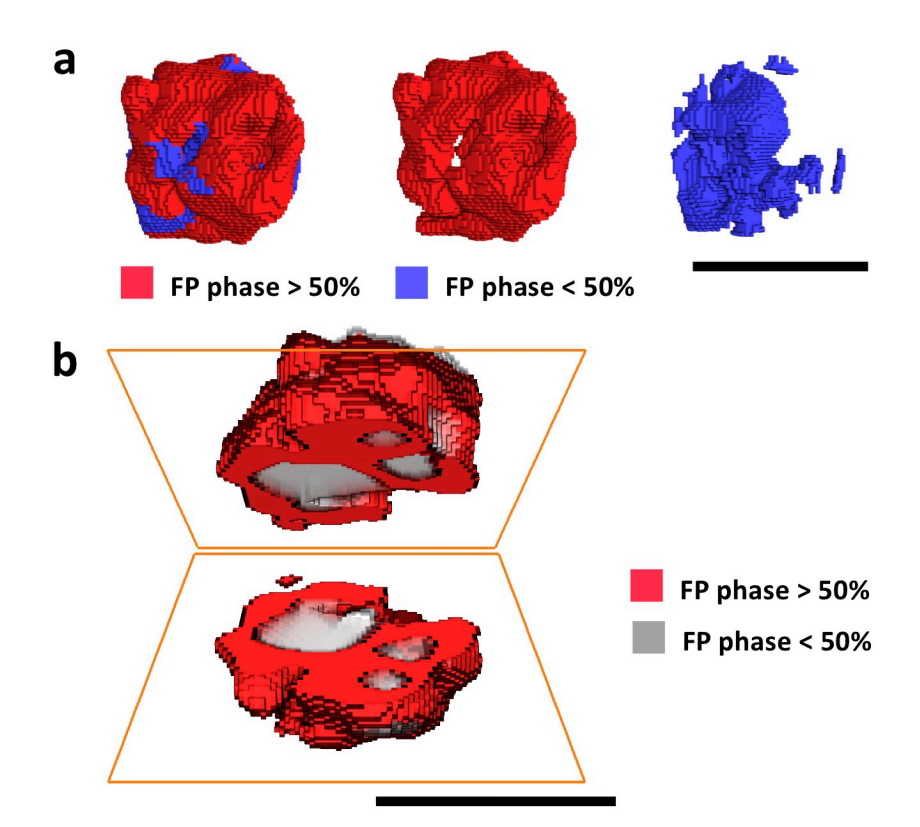
**Supplementary Figure S4. 3D phase mapping in partially delithiated LFP secondary particles. a, b)** Distribution of local LFP/FP phase fraction in the secondary particles shown in Figure 2a and 2b, respectively. Voxels containing FP (or LFP) phase only are shown in red (or blue), and voxels that contain both LFP and FP phases have intermediate colors.



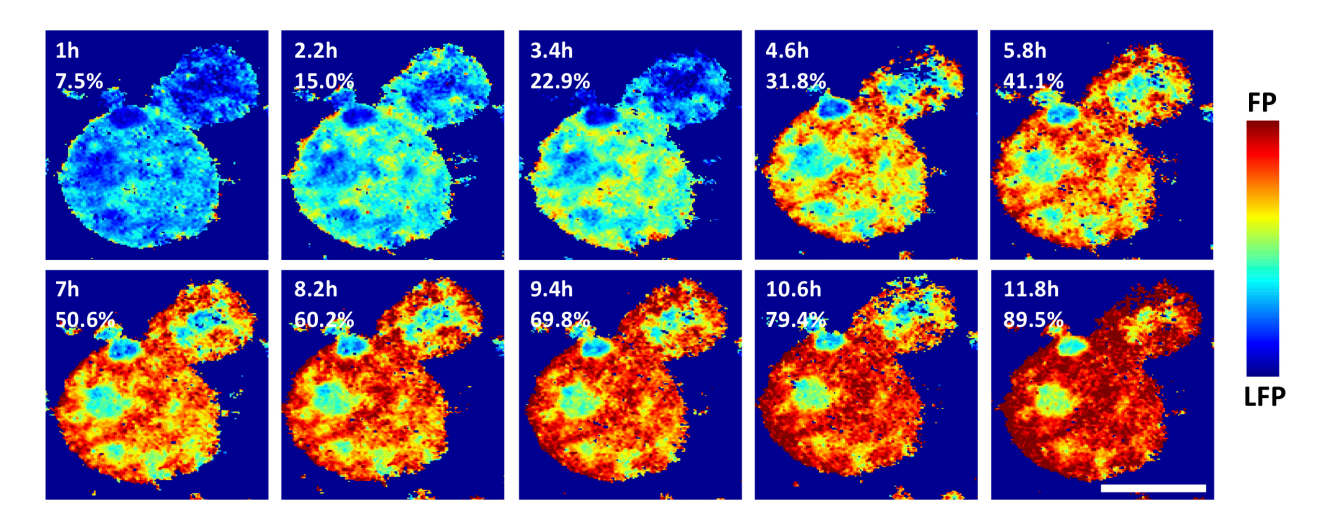
Supplementary Figure S5. Phase distribution in an LFP secondary particle with local SOC = 6% from an electrode charged at the 2C rate. a) Separate visualization of the FP (red volume) and LFP (blue volume) domains in the particle. b) Dissecting view of the phase distribution inside the particle with the LFP phase in semi-transparent gray color. Scale bars are  $2 \mu m$ .



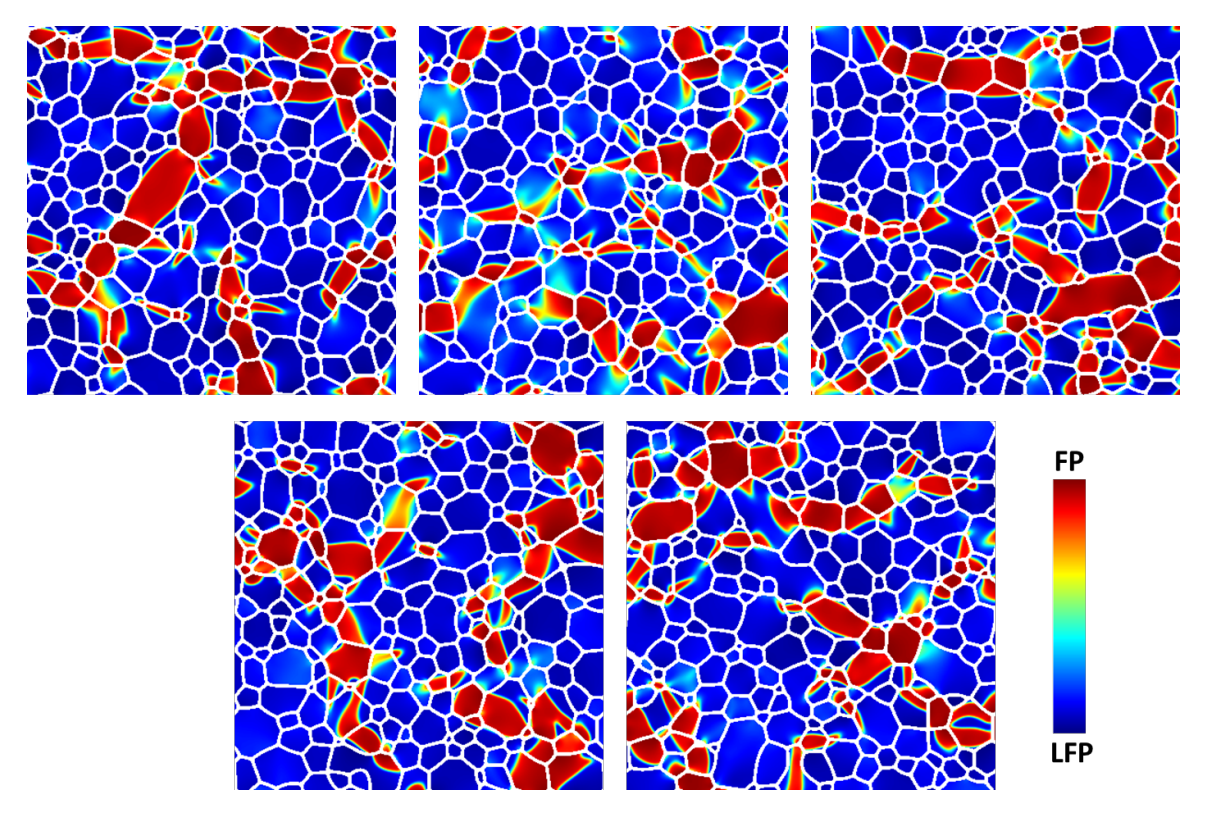
Supplementary Figure S6. Phase distribution in an LFP secondary particle with local SOC = 30% from an electrode charged at the 2C rate. a) Separate visualization of the FP (red volume) and LFP (blue volume) domains in the particle. b) Dissecting view of the phase distribution inside the particle with the LFP phase in semi-transparent gray color. White arrow points to an FP filament that extends into the particle interior. Scale bars are  $2 \mu m$ .



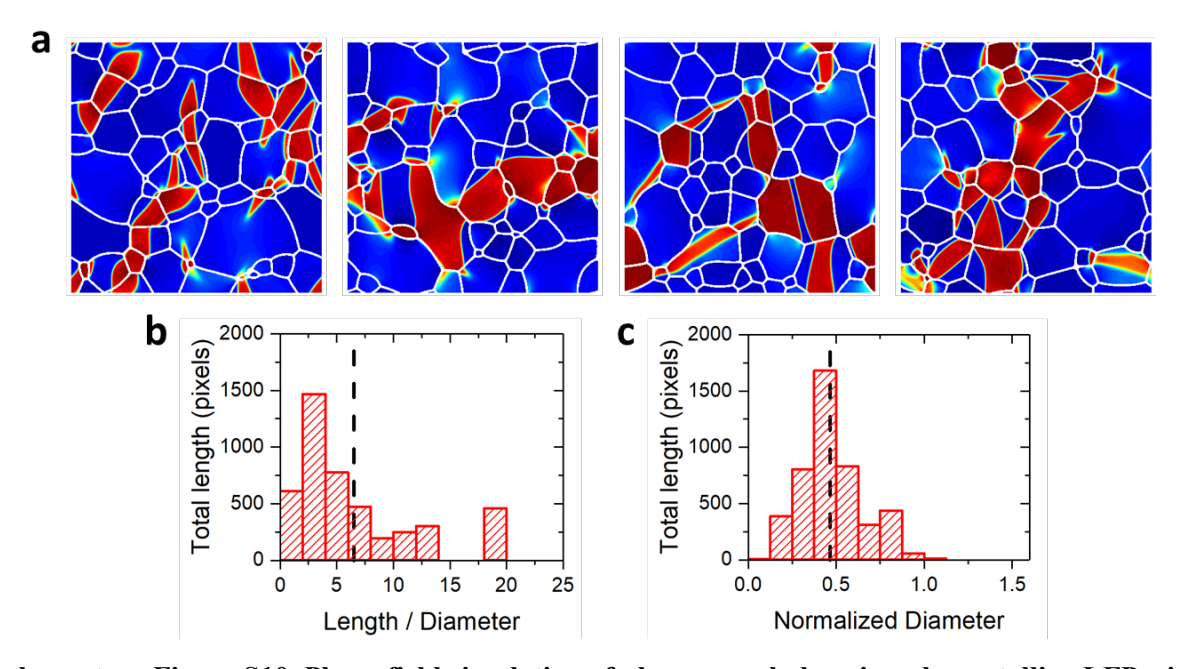
Supplementary Figure S7. Phase distribution in an LFP secondary particle with local SOC = 63% from an electrode charged at the 2C rate. a) Separate visualization of the FP (red volume) and LFP (blue volume) domains on the particle. b) Dissecting view of the phase distribution inside the particle with the LFP phase in semi-transparent gray color, which shows that FP and LFP phases form a core-shell structure. Scale bars are 2  $\mu$ m.



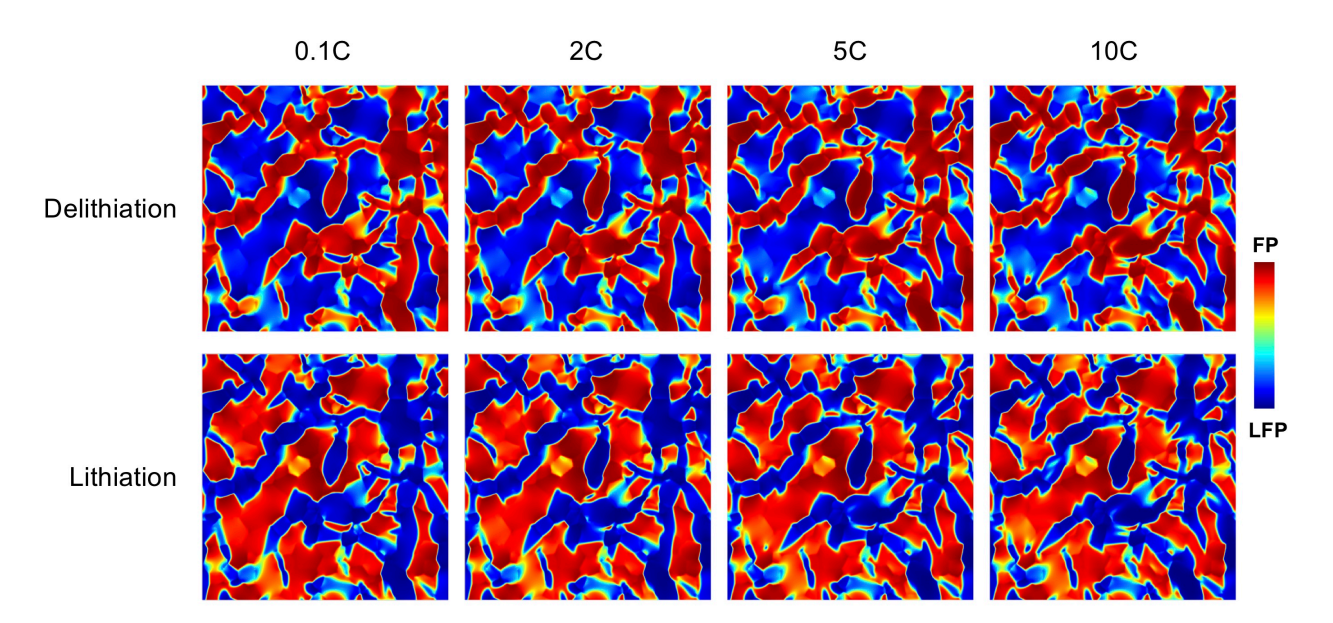
Supplementary Figure S8. Operando 2D XANES imaging of a secondary particle in an LFP electrode during potentiostatic charging at 3.46 V. Time and the corresponding SOC of the secondary particle are shown in each TXM image. Scale bar: 10 µm.



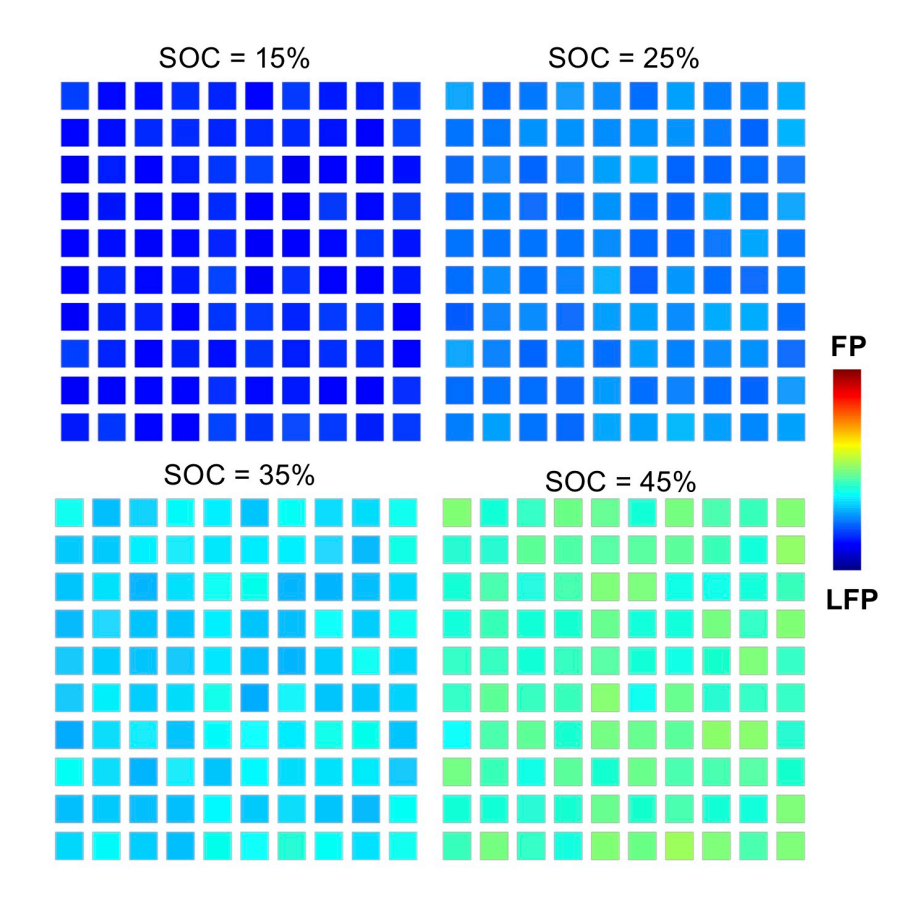
Supplementary Figure S9. Simulated phase distributions in five different polycrystalline LFP configurations charged to SOC 30% at the 0.1C rate. All configurations consist of 200 grains.



**Supplementary Figure S10. Phase-field simulation of phase morphology in polycrystalline LFP with larger grain sizes. a)** Simulated two-phase structure in four different polycrystalline LFP configurations (400 nm × 400 nm) charged to 30% SOC at 0.1C, all of which have an average grain size of 64 nm and contain 50 grains. **b, c)** Histograms of the FP filament length/diameter ratio and diameter normalized by average grain size at 30% SOC, respectively, based on the filament tracing analysis of the simulated FP domain structure. The black dashed lines in **b** and **c** represent the means. The average length-to-diameter ratio of the FP filaments is 6.5, and the average filament diameter is 0.46 times of the mean grain size.



Supplementary Figure S11. Simulated phase distributions in a 2D polycrystalline LFP system delithiated or lithiated to 50% SOC at different C rates. The two-phase morphology is independent of (dis)charging rate and symmetric between charging and discharging, i.e. the phase distributions in the delithiated and lithiated systems are the complements of each other.



**Supplementary Figure S12.** Concurrent Li intercalation in a system of separated LFP nanoparticles upon discharging at the 5C rate. The dimension of the square-shaped particles is equal to the average grain size of the polycrystal configuration shown in Figure 5 and Supplementary Figure S7. In the simulation, traction-free boundary condition is applied to the particle surface, and so the particles do not interact with each other elastically. The initial Li concentration in each particle is randomly distributed between 0.05 and 0.15. Snapshots of the system at SOC = 15%, 25%, 35% and 45% show that all of the particles simultaneously intercalate Li.

#### References

- 1. M. Y. Ge, W. K. Lee. PyXAS an Open-Source Package for 2D X-Ray Near-Edge Spectroscopy Analysis. *Journal of Synchrotron Radiation* **27**, 567 (2020).
- 2. N. Moelans, B. Blanpain, P. Wollants. Quantitative Analysis of Grain Boundary Properties in a Generalized Phase Field Model for Grain Growth in Anisotropic Systems. *Physical Review B* **78**, 024113 (2008).
- 3. M. Tang, J. F. Belak, M. R. Dorr. Anisotropic Phase Boundary Morphology in Nanoscale Olivine Electrode Particles. *Journal of Physical Chemistry C* **115**, 4922 (2011).
- 4. K. Q. Yang, M. Tang. Three-Dimensional Phase Evolution and Stress-Induced Non-Uniform Li Intercalation Behavior in Lithium Iron Phosphate. *Journal of Materials Chemistry A* **8**, 3060 (2020).
- 5. N. Meethong, H. Y. S. Huang, S. A. Speakman, W. C. Carter, Y. M. Chiang. Strain Accommodation during Phase Transformations in Olivine-Based Cathodes as a Materials Selection Criterion for High-Power Rechargeable Batteries. *Advanced Functional Materials* 17, 1115 (2007).
- 6. T. Maxisch, G. Ceder. Elastic Properties of Olivine Li<sub>x</sub>FePO<sub>4</sub> From First Principles. *Physical Review B* **73**, 174112 (2006).
- 7. A. Abdellahi, O. Akyildiz, R. Malik, K. Thornton, G. Ceder. Particle-Size and Morphology Dependence of the Preferred Interface Orientation in LiFePO<sub>4</sub> Nano-Particles. *Journal of Materials Chemistry A* **2**, 15437 (2014).
- 8. G. K. Singh, G. Ceder, M. Z. Bazant. Intercalation Dynamics in Rechargeable Battery Materials: General Theory and Phase-Transformation Waves in LiFePO4. *Electrochimica Acta* **53**, 7599 (2008).
- 9. D. A. Cogswell, M. Z. Bazant. Coherency Strain and the Kinetics of Phase Separation in LiFePO<sub>4</sub> Nanoparticles. *ACS Nano* **6**, 2215 (2012).
- 10. L. Hong, K. Q. Yang, M. Tang. A Mechanism of Defect-Enhanced Phase Transformation Kinetics in Lithium Iron Phosphate Olivine. *NPJ Computational Materials* **5**, 118 (2019).
- 11. J. W. Cahn, J. E. Hilliard. Free Energy of a Nonuniform System .1. Interfacial Free Energy. *Journal of Chemical Physics* **28**, 258 (1958).
- 12. J. W. Cahn. On Spinodal Decomposition. *Acta Metallurgica* **9**, 795 (1961).
- 13. D. Morgan, A. Van der Ven, G. Ceder. Li Conductivity in  $Li_xMPO_4$  (M = Mn, Fe, Co, Ni) Olivine Materials. *Electrochemical and Solid-State Letters* 7, A30 (2004).
- 14. Y. J. Zhu, C. S. Wang. Galvanostatic Intermittent Titration Technique for Phase-Transformation Electrodes. *Journal of Physical Chemistry C* **114**, 2830 (2010).
- 15. J. Lim, Y. Y. Li, D. H. Alsem, H. So, S. C. Lee, P. Bai, D. A. Cogswell, X. Z. Liu, N. Jin, Y. S. Yu, N. J. Salmon, D. A. Shapiro, M. Z. Bazant, T. Tyliszczak, W. C. Chueh. Origin and Hysteresis of Lithium Compositional Spatiodynamics Within Battery Primary Particles. *Science* **353**, 566 (2016).